T.R.
BOLU ABANT İZZET BAYSAL UNIVERSITY
INSTITUTE OF GRADUATE STUDIES
Department of Physıcs

FULL CHARACTERIZATION OF Sr SITE Nd SUBSTITUTED BULK Bi-2223 SUPERCONDUCTING SAMPLES WITH STANDARD EXPERIMENTAL METHODS AND THEORETICAL APPROACHES

DOCTOR OF PHILOSOPHY

MUSA DOĞRUER

ACADEMIC SUPERVISOR
Prof. Dr. Cabir TERZİOĞLU
ACADEMIC CO-SUPERVISOR
Assoc. Prof. Dr. Gürcan YILDIRIM

BOLU, JUNE- 2021

APPROVAL OF THE THESIS

Full Characterization of Sr Site Nd Substituted Bulk Bi-2223 Superconducting Samples with Standard Experimental Methods and Theoretical Approaches submitted by **Musa DOĞRUER** and defended before the Examining Committe Members listed below in partial fulfillment of the requirements for the degree of **Doctor of Philosophy** in **Department of Physics, Institute of Graduate Studies of Bolu Abant Izzet Baysal University in 21.06.2021** by

Examining Committee Members	Signature
Supervisor Prof. Dr. Cabir TERZİOĞLU Bolu Abant Izzet Baysal University	....
Member Prof. Dr. Osman GÖRÜR Bolu Abant Izzet Baysal University	....
Member Prof. Dr. Özgür ÖZTÜRK Kastamonu University	....
Member Prof. Dr. Ahmet Tolga TAŞÇI Kastamonu University	....
Member Prof. Dr. Cihan PARLAK Bolu Abant Izzet Baysal University	....

Prof. Dr. Osman GÖRÜR

Director of Instıtute of Graduate Studies

ETHICAL DECLARATION

In this thesis dissertation that was properly prepared according to the Thesis Writing Rules of Bolu Abant İzzet Baysal University of the Institute of Graduates Studies, I hereby declare that;

- All data, information, and documents presented in the thesis were obtained in accordance with the academic and ethical rules,
- All data, documents, assessments, and results were presented in accordance with the scientific ethical and moral rules,
- All works that were benefitted in the thesis were appropriately cited,
- No alteration was made in the data used,
- Study presented in this thesis is original,

Otherwise, I declare that I accept the loss of all my rights in case any contradiction that may arise against me.

Based on the plagiarism report that was generated on the date of 15/06/2021 by using predetermined filtrations set by Directorate of Institute of Graduate Studies of the Turnitin programme, a plagiarism detection sofware, the rate of plagiarism detected was 22 %.

____

Musa DOĞRUER

ABSTRACT

FULL CHARACTERİZATİON OF SR SİTE ND SUBSTİTUTED BULK Bİ-2223 SUPERCONDUCTİNG SAMPLES WİTH STANDARD EXPERİMENTAL METHODS AND THEORETİCAL APPROACHES
PHD THESIS
MUSA DOĞRUER
BOLU ABANT IZZET BAYSAL UNIVERSITY
INSTITUTE OF GRADUATE STUDIES
DEPARTMENT OF PHYSICS
(SUPERVISOR: PROF. DR. CABİR TERZİOĞLU)
(CO-SUPERVISOR: ASSOC. PROF. DR. GÜRCAN YILDIRIM)
BOLU, JUNE 2021
Number of pages in Roman and Arabic numerals (xiii + 70)

The aim of this thesis is to examine the very significant properties including the electrical, structural, mechanical, flux pinning mechanism and superconducting in the Bi-2223 system with the partial replacement of neodymium foreign particles by strontium impurity. Superconducting materials prepared by standard solid-state route at the sintering temperature of 840 °C for 48 h are carried out by experimental measurement methods such as X-Ray diffraction analysis, scanning electron microscopy, electron dispersive X-Ray, Vickers microhardness, resistivity and magnetization measurements. For the industrial and technological applications, the significant properties such as the normal state resistivity, critical transition temperature, crystallinity, phase purity, lattice parameter, texturing, surface morphology and Vickers microhardness are obtained for all samples and compared with each other. The pure sample displays the high-T_c Bi-2223 superconducting phase the 97.55 % volume fraction level. Further, the volume fraction value of high-T_c Bi-2223 phase decrease from 94.43 % in level x=0.01 sample to 26.65 % for the level of x = 0.1. Lattice constant *a* increases while lattice constant *c* decrease with increasing in Nd additives. While the maximum offset critical temperature of the pure sample is 108.4 K, a minimum of 78.81 K is obtained for the level of x = 0.1. All the theoretical approaches and experimental results display the characteristic properties tend to deteriorate with the increase in the Nd impurity.

KEYWORDS: Nd substituted Bi-2223, Pinning mechanism, XRD, SEM, H_v.

ÖZET

SR TABAKASI ND YER DEĞİŞTİRİLMİŞ BULK Bİ-2223 SÜPERİLETKEN ÖRNEKLERİN STANDART DENEYSEL YÖNTEMLER VE TEORİK YAKLAŞIMLAR İLE TAM KARAKTERİZASYONU
DOKTORA TEZİ
MUSA DOĞRUER
BOLU ABANT İZZET BAYSAL ÜNİVERSİTESİ
LİSANSÜSTÜ EĞİTİM ENSTİTÜSÜ
FİZİK ANABİLİM DALI
(TEZ DANIŞMANI: PROF. DR. CABİR TERZİOĞLU)
(İKİNCİ DANIŞMAN: DOÇ. DR. GÜRCAN YILDIRIM)
BOLU, HAZİRAN- 2021
Roma ve Arap rakamları ile tez sayfa sayıları (xiii + 70)

Bu tezin amacı, neodim yabancı partiküllerin stronsiyum safsızlığı ile kısmen yer değiştirmesi ile Bi-2223 sistemindeki elektriksel, yapısal, mekanik, akı sabitleme mekanizması ve süperiletken gibi çok önemli özellikleri araştırmaktır. Standart katı hal yolu ile 840 °C tavlama sıcaklığında 48 saatte hazırlanan süperiletken malzemeler X-ışını kırınım analizi, taramalı elektron mikroskobu, elektron dağılımlı X-ışını, Vickers mikrosertlik, özdirenç ölçümleri ve mıknatıslanma gibi deneysel ölçüm yöntemleriyle gerçekleştirilir. Endüstriyel ve teknolojik uygulamalar için normal durum direnci, kritik geçiş sıcaklığı, kristallik, faz saflığı, kafes parametresi, doku, yüzey morfolojisi ve Vickers mikro sertliği parametreleri gibi önemli özellikler tüm numuneler için elde edilmiş ve birbirleriyle karşılaştırılmıştır. Saf numune, yüksek T_c Bi-2223 süper iletken fazını % 97.55 hacim fraksiyon seviyesini gösterir. Ayrıca, yüksek T_c Bi-2223 fazının hacim fraksiyon değeri, x = 0.01 numunesinde % 94.43'ten x = 0.1 seviyesi için % 26.65'e düşer. Örgü sabiti *a* artarken, örgü sabiti *c* Nd katkı maddelerinde artışla azalır. Saf numunenin maksimum ofset kritik sıcaklığı 108.4 K iken, x = 0.1 seviyesi için minimum 78.81 K elde edilir. Tüm teorik yaklaşımlar ve deneysel sonuçlar, karakteristik özelliklerin Nd safsızlığındaki artışla bozulma eğiliminde olduğunu göstermektedir.

ANAHTAR KELİMELER: Nd ikameli Bi-2223, Sabitleme mekanizması, XRD, SEM, H_v.

TABLE OF CONTENTS

LIST OF FIGURES

Page

LIST OF TABLES

Page

LIST OF ABBREVIATIONS AND SYMBOLS

a, c	: Lattice Parameters
B	: Brittleness Index
BCS	: Bardeen, Cooper, Schrieffer Theory
Bi_2O_3	: Bismuth (III) Oxide
BSCCO	: Bismuth Strontium Calcium Copper Oxide
$CaCO_3$	: Calcium Carbonate
CuO	: Copper (II) Oxide
C_{11}	: Elastic Stiffness
Dc	: Direct Current
E	: Elastic Modulus
EDX	: Energy Dispersive X-ray Spectroscopy
EPD	: The elastic / plastic deformation model
f_I	: Volume fraction
h	: Hours
HBCCO	: Mercury Bismuth Calcium Copper Oxide
H_c	: Critical Magnetic Field
H_{c1}	: Irreversible Critical Field
H_{c2}	: Upper Critical Field
hkl	: Miller Indices
HK	: Hays Kendall approach
H_v	: Vickers Hardness
I	: Intensity
IIC	: Indentation Induced Cracking Model
ISE	: Indentation Size Effect
K	: Kelvin
k_B	: Boltzmann's Constant
K_{IC}	: Fracture Toughness
LBCO	: Lanthanum Barium Copper Oxide
M	: Magnetization
MgB_2	: Magnesium Diboride
min	: Minute
MPSR	: Modified Proportional Sample Resistance

MRI	: Magnetic Resonance Imaging
n	: Meyer Number
NbN	: Niobium Nitride
Nb_3Ge	: Niobium-Germanium
Nd_2O_3	: Neodymium (III) Oxide
NMR	: Nuclear magnetic resonance
P	: Hole Carrier Concentrations
PbO	: Lead (II) Oxide
PSR	: Proportional Specimen Resistance
R	: Resistance
RF	: Radio Frequency
s	: Second
SEM	: Scanning Electron Microscope
$SrCO_3$	: Strontium Carbonate
SQUIDS	: Superconducting Quantum Interference Device
T	: Temperature
TAFF	: Thermally Activated Flux Flow
TBCCO	: Thallium Barium Calcium Copper Oxide
T_c^{offset}	: Offset Critical Transition Temperature
T_c	: Critical Temperature
T_c^{onset}	: Onset Critical Transition Temperature
U_0	: Pinning Energy
V_F	: Fermi Velocity
Y	: Yield Strength
YBCO	: Yttrium Barium Copper Oxide
XRD	: X-ray Diffraction
Θ_B	: Bragg Angle
Å	: Angstrom Unit
^oC	: Celsius Degree
ρ_{300}	: Room Temperature Resistivity
ħ	: Planck Constant
κ	: Ginzburg-Landau Coefficient
ξ	: Coherence Length
Δ	: Gap Parameter

ΔT_c	**:** Transition Width
λ	**:** Penetration Depth
$\mu_0 H_{irr}$	**:** Irreversibility Fields
$\mu_0 H_{c2}$	**:** Upper Critical Fields
β	**:** Full Width at Half Maximum

ACKNOWLEDGEMENTS

The author wishes to express his deepest gratitude to his supervisor Prof. Dr. Cabir TERZİOĞLU and co-supervisor Assoc. Prof. Dr. Gürcan YILDIRIM for their guidance, advice, criticism, encouragements and insight throughout the research.

1. INTRODUCTION

Helium liquefied for the first time in 1908 by Kammerling Onnes. Then, electrical resistance in pure mercury was suddenly in 1911 disappeared under a critical temperature (T_c = 4.2 K) (1). Shortly afterwards, the same influence was observed in indium (3.4 K), tin (3.72 K) and in lead (7.19 K). Superconductivity critical temperature in niobium was found 9.2 K in 1930 in and NbN was obtained 17 K in 1940. In 1973, the Nb_3Ge compound, achievable in liquid hydrogen, was found in critical temperature of 23.2 K. In 1934, the F. and H. London suggested equations that describe the Meissner effect and the forecasted the depth of penetration of a static magnetic field into the surface of a superconductor (2). In 1950, Ginzburg and Landau theory was appeared to be accomplish and can give knowledge about characteristic of superconducting materials. Alexei Abrikosov discovered distinguish two sorts of superconducting material: type-I and type-II superconductors (3). Although the magnetic flux expels from the inner of type-I, the type-II does it only at minor fields, but in greater exterior fields. Type-II materials, called mixed states, that can maintain superconductivity in fields upper than 10 Tesla are of interest for large scale application. In 1986, LBCO (La-Ba-Cu-O) compound is the first oxide based on high T_c superconductor and critical temperature is obtained as 36 K (4). LBCO is the first high T_c superconductor to overcome the 30 K barrier brought by the BCS theory. In 1987, K. Wu and Paul Chu was discovered YBCO ceramics at T_c - 92 K. This was a significant discovery for superconductivity with a critical temperature beyond liquid nitrogen, which is less expensive than liquid helium (5). In 1987, the first high T_c superconducting BSCCO compound was found and does not contain a rare earth element (6). There are three different phases in BSCCO superconductor are called 2201, 2212 and 2223 according to their composition ($Bi_2Sr_2Ca_{n-1}Cu_nO_{2n+4+x}$) and their critical temperatures are 20 K, 85 K and 110 K, respectively (7, 8). TBCCO was discovered in 1988. Chemical composition is $Ti_2Ba_2Ca_{n-1}Cu_nO_{2n+4+x}$ with critical temperature as T_c=85 K (n=1, 2201 phase), 110 K (n=2, 2212 phase) and 127 K (n=3, 2223 phase) (9, 10). In 2009, HBCCO (Hg-Ba-Ca-Cu-O) is the highest member of high T_c superconductor family until today. The composition of the system is $Hg_1Ba_2Ca_{n-1}Cu_nO_{2n+2+x}$ with critical temperature as T_c=94 K (n=1, 1201 phase), 128 K (n=2, 1212 phase) and 134 K (n=3, 1223 phase) (11, 12). The MgB_2 material (13) has properties of its crystal structure, low density, large coherence length, simple chemical composition low anisotropy, light weight and weak-link-free grain connection.

1.1 Meissner Effect

Meissner and Ochsenfeld discovered second distinct feature of superconductor as called perfect diamagnetism in 1933 (14). According to this superconducting property, in external magnetic fields, magnetic flux is ejected from the inside of the sample that is cooled under the critical temperature (Figure. 1.1)

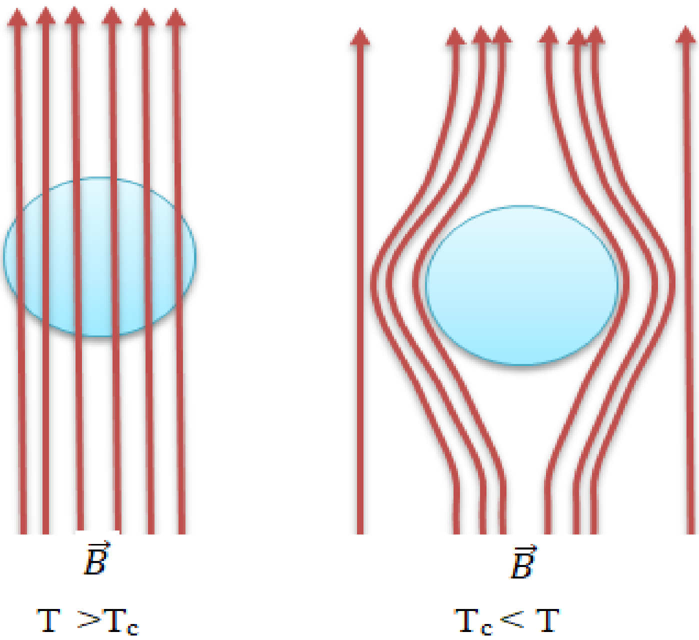

Figure 1.1. The exclusion of weak exterior magnetic field from inside of superconductor.

1.2 Types of Superconductors

Alexei Abrikosov discovered distinguish two sorts of superconducting material: type-I and type-II superconductors in 1957. In type-I superconductors, when magnetic flux rises beyond a critical magnetic field, they are destroyed the superconductivity and materials became totally normal (Figure 1.2). On the other hand, a Type II superconductor obeys very differently. The magnetic field starts to penetrate at an irreversible critical field (H_{cl}) and continues to rise with increments in the applied field till it achieves the value of the upper critical field (H_{c2}), after which the entire material turns to normal state. There is no flux penetration for applied fields below H_{cl}, this is called Meissner state. According to the Figure 1.3, there is a mixed state with areas of nonsuperconducting material inserted in a perfectly superconducting matrix between critical fields H_{cl} and H_{c2} (15).

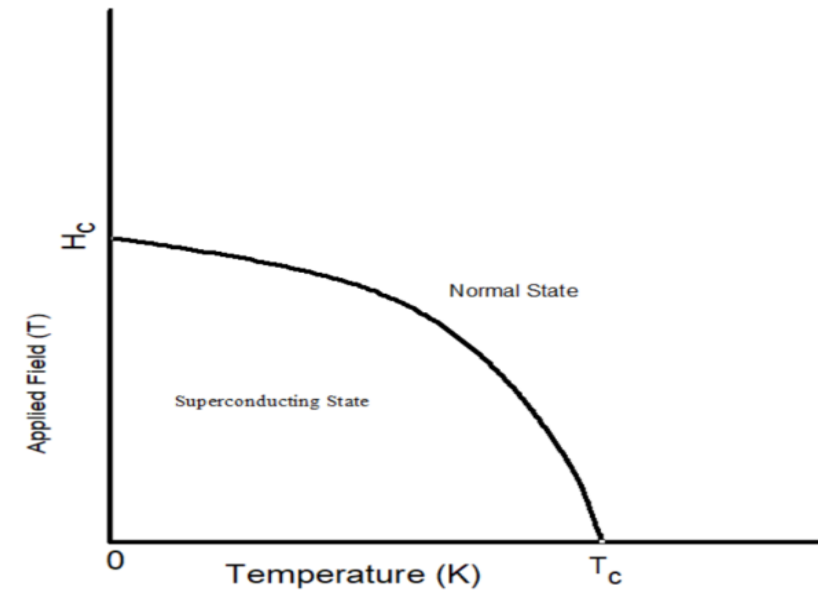

Figure 1.2. H_c (T) representation graph for type I superconductor.

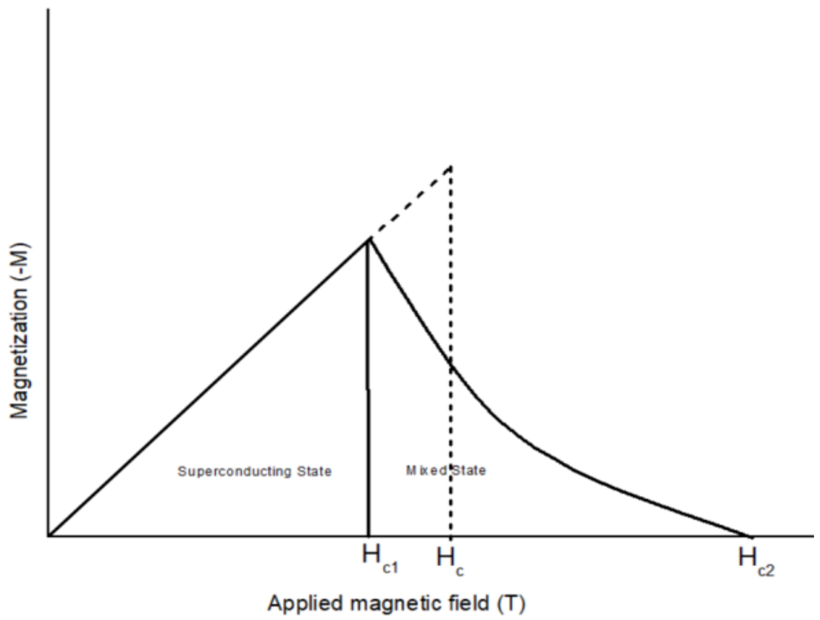

Figure 1.3. Magnetization against applied magnetic field for type II superconductor.

1.3 Josephson Effect

In 1962, Josephson suggested a quantum tunneling influences that can occur when a super-current tunnel through thin layer of an insulator. The zero-voltage current flow causing from tunnelling of Cooper pairs is called dc Josephson Effect. Further, Josephson proposed that a supercurrent will flow through the barrier producing dc current by the tunnelling of single electrons at constant nonzero voltage. Josephson has two effects, tunnelling junctions and weak links. In ac Josephson Effect, RF voltage in combination with dc voltage can cause direct current flow through the junction. Therefore, this influence has been used to measure e / h very indeed and can be used as a tool to establish a voltage standard (16).

1.4 BCS Theory

In 1957, Bardeen, Cooper and Schrieffer have suggested a microscopic superconductivity theory, called the BSS theory. In normal state, the electrons repulse each other with Coulomb force; however, at low temperature there is a net attraction between two electrons called Cooper pairs. In BCS theory, resistance goes to zero in the stability of a single state, where the possibility waves of electron couples move without scattering through a lattice. The lattice vibration mechanism is known as phonon in terms of Cooper pairs in BCS theory. Further, the theory can explain the presence of a critical field. This applied magnetic field provides sufficient energy to breaks up the Copper couples. The interaction of small magnets of coupled electrons with the field separates a Copper pair. As the temperature drops below Tc, the superconducting gap and hence the coupling energy of the couple increments; therefore, the critical field increases as the temperature decreases. Moreover, the BCS theory describes the beginning of the magnetic field interior the superconductor. There are thin thread filaments with normal conductivity known as vortex in the Type II superconductor (17).

1.5 Penetration Depth

There is no magnetic field inside of superconductor at Meissner state, but at the surface of material this cannot be true. Obviously, to cancel ***B*** needs currents on the surface cause to magnetization (M) consequently inside of the superconductor is $M+H = 0$. These currents of surface do not disperse energy because the resistivity is zero and this is called supercurrents. The thickness estimated from the surface on which supercurrents flow is called the penetration depth (18) (Figure 1.5).

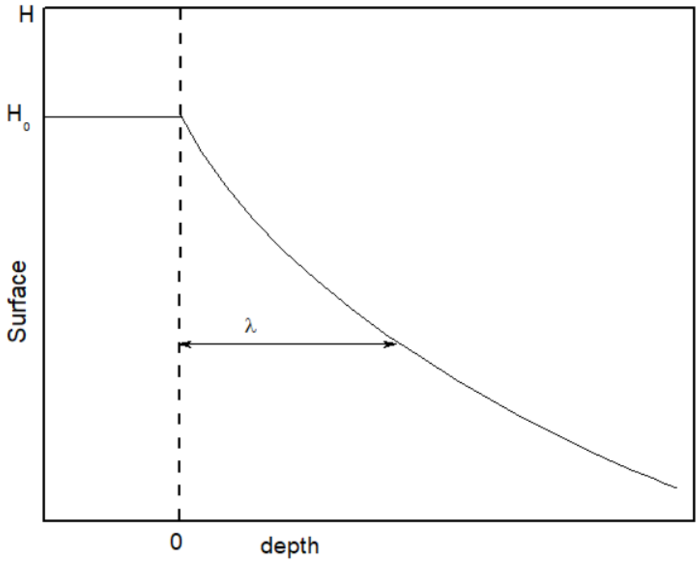

Figure 1.4. Schematic distortion of the magnetic field inside a superconductor.

1.6 Coherence Length

The coherence length (ξ) is the distance between two electrons of the Cooper pair. Another definition of the coherence length is a measure of the distance at which the gap parameter (Δ) can differ in a changing magnetic field (19). Further, we calculate the BCS coherence length (ξ_0) which is associated to the Fermi velocity (***v_F***) and the energy gap by the formula:

$$\xi_0 = \frac{\hbar v_F}{\pi \Delta} \tag{1.1}$$

1.7 The Ginzburg-Landau Coefficient

The penetration depth and coherence length ratio are called the Ginzburg-Landau ratio ($\kappa = \lambda/\xi$). The κ value allows to differentiate between type-I and type-II superconductors. As material exceeds 0.7 (κ > 0.7), it has the type-II superconductor. If κ < 0.7, a material is dealing with type-I superconductor (19, 20).

1.8 Applications of Superconductivity

Important advances have been made in the applications related to superconducting electronics and superconducting wires and tapes. Radio astronomy receivers, wireless communication systems, microwave filters, NMR microchips, MRI coils, SQUIDS (Superconducting Quantum Interference Devices) and digital instruments are among electronic applications. Generators, motors, transformers, current limiters, magnetic energy storage, power transmission lines, magnetic separation, current cables and research magnet systems are applications of superconducting wires and cables.

1.9 Structure and Dropping/Substitution of BSCCO System

According to chemical composition of $Bi_2Sr_2Ca_{n-1}Cu_nO_y$ formula, there are three various phases. The n = 1 of the series is $Bi_2Sr_2Cu_1O_{6+\delta}$ (2201), for which T_c is ~20 K. The n = 2 phase $Bi_2Sr_2CaCu_2O_{8+\delta}$ (2212), has a T_c of ~ 85 K, and n = 3 compound $Bi_2Sr_2Ca_2Cu_3O_{10+\delta}$ (2223), is a T_c of 110 K (21). Figure 1.6-1.8 (22) shows the crystal structure of 2201, 2212 and 2223 compounds, respectively. The 2201 phase includes one $Cu\text{-}O_2$ layer surrounded by two Sr-O and Bi-O layers, respectively. In the 2201 system without Ca layer, Cu atoms of the octahedral structure with the closest six O atoms are formed. Further, the 2212 phase is described by two $Cu\text{-}O_2$ layers with one Ca sandwiches and the 2223 phase are consisting of three $Cu\text{-}O_2$ layers with two sheets of Ca interleaves. While Cu atoms form a pyramid structure with five O atoms in 2212 material, together with the pyramid structure in phase 2223, its form square layers with four O atoms. The *c* axis length parameters of the three phases are 24.6 Å, 30.7 Å and 37.1 Å for 2201, 2212 and 2223 phases, respectively, while the *a* axis length parameter is 5.4 Å for all phases.

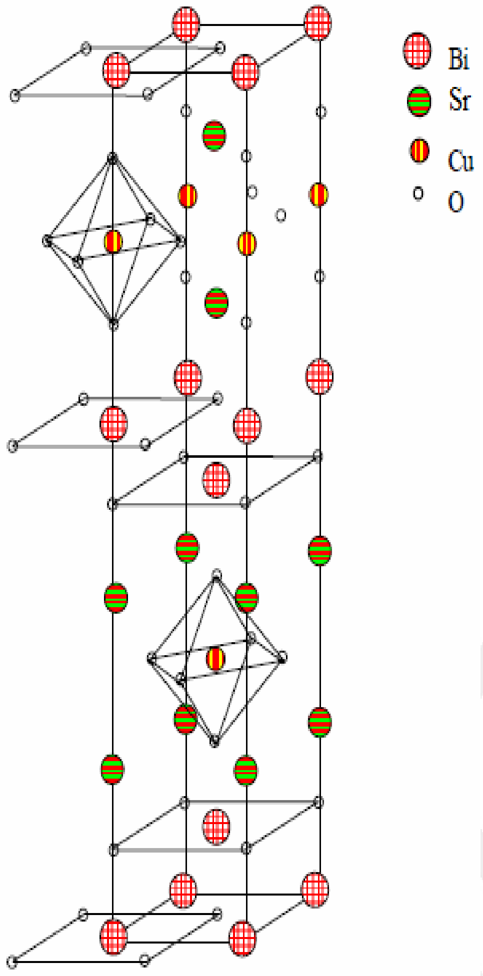

Figure 1.5. Crystalline structure of Bi-2201 superconductor.

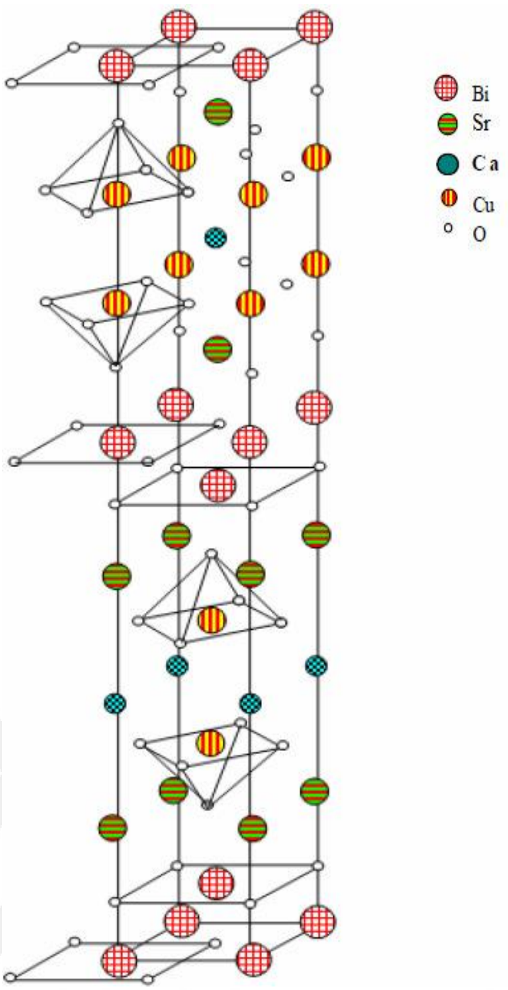

Figure 1.6. Crystalline structure of Bi-2212 superconductor.

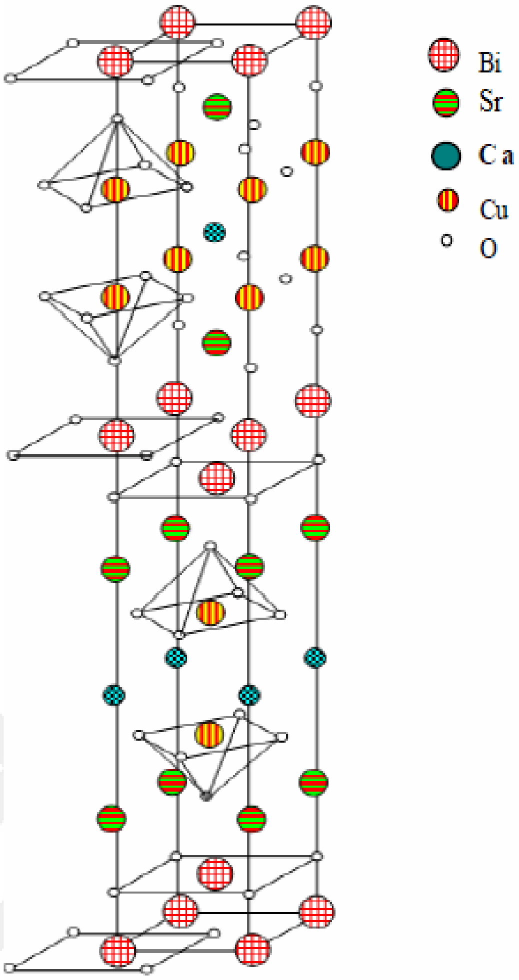

Figure 1.7. Crystalline structure of Bi-2223 superconductor.

2. AIM AND SCOPE OF THE STUDY

Many Bi-based superconducting materials are generated chemical doping with different oxides/elements and particles addition/substitution to develop their electrical, microstructural, mechanical and flux pinning properties. There are many dropping/substitution research were performed in 2223 compound. Bi-based compounds with easy and quick phase formation (no requirement high pressure or for a gas other than air atmosphere), thermodynamic stability, cheap and harmless chemical contents show the without gain or oxygen loss under greater annealing temperature as 850 ºC can be as displayed for the industrial applications and engineering (23–25). Further, the 2223 phase is most useful as a result of its phase stability, magnetic field, highest T_c and current carrying capacities applications in the technology (26). Nevertheless, some limitations regarding the structural sheets, great penetration depths, tremendously brittleness, short coherence lengths, low charge carrier densities, restricted range of temperatures and extreme magnetic fields obstruct research of 2223 compound.

In the present work, we investigate the effect of aliovalent Nd/Sr partial replacement in the crystal structure on the electrical, mechanical, superconducting, crystal structure quality, physical, flux pinning mechanism, electronic structures, and microstructural quality of high-T_c Bi-2223 superconducting material by means of temperature-dependent resistivity (ρ-T), Vickers Microhardness (H_v), powder X-ray diffraction (XRD), magnetization (M-H), scanning electron microscopy (SEM) and electron dispersive X-ray (EDX) experimental measurements so that the bulk Bi-2223 superconducting ceramic materials can find much more application fields in the advanced engineering and large-scale areas. For the industrial and technological applications, the crucial features such as the electrical results, characteristic critical transition temperatures, crystallinity quality, reaction kinetics, texturing, lattice parameter, crystal structure quality, grain alignment distributions, surface morphology appearance and Vickers microhardness values are found for the pure and Nd substituted samples and compared with each other.

3. MATERIALS AND METHODS

3.1 Solid State Method

There are many processing stages to produce superconductor materials. To obtain perfect phases, the desired samples must be dense, lower porosity, larger grains, and well-defined microstructures. Solid state techniques are usually based on powder synthesis, mixing of stoichiometric oxides, grinding, forming, pressing, and annealing.

3.1.1 Weighing

Weighing different powders according to stoichiometry is the first step in the solid-state reaction method. The existence of purities in the materials can damage the superconductor properties. In this study, we used $SrCO_3$, Nd_2O_3, PbO, Bi_2O_3, $CaCO_3$, CuO chemicals with purity of 99.9%. The amounts of chemicals are weighed with the help of an electronic balance that provides accuracy up to five decimal places in grams. The following balancing equation is used to determine the appropriate amounts of the powders.

$$(0.90)\ Bi_2O_3 + (0.35)\ PbO + (1.9-y)\ SrCO_3 + (2.2)\ CaCO_3 + (3)\ CuO + (y/2)\ Nd_2O_3 \rightarrow Bi_{1.8}Pb_{0.35}Sr_{1.9-y}Nd_yCa_{2.2}Cu_3O_x$$

The series of Sr-substituted Bi-2223 superconducting compounds are produced by the partial replacement of Nd-sites in the system according to nominal composition of $Bi_{1.8}Pb_{0.35}Sr_{1.9-y}Nd_yCa_{2.2}Cu_3O_x$ (where y= 0.00, 0.01, 0.03, 0.05, 0.07 and 0.10 are shown as the pure, Nd1, Nd2, Nd3, Nd4 and Nd5, respectively) with the aid of standard solid-state reaction method known to be based on powder synthesis, mixing of stoichiometric oxides, grinding, forming, pressing and annealing processes.

3.1.2 Grindings and Calcinations

Calcination causes chemical decomposition and reaction among different elements to form the compound. Temperature, heating time and atmosphere are important features that define calcination conditions. The process that mechanically divides solid particles into fine particles is called grinding. Medium grinding prepares the chemical material for further processing. Further, the grinding can decrease the compositional differences that might still arise because of calcination. The $SrCO_3$, Nd_2O_3, PbO, Bi_2O_3, $CaCO_3$, CuO chemicals are mixed for 24 h in a grinding machine to attain homogeneous mixture. The ground and homogenized powders are calcined firstly at a temperature of 750 ºC for about 12 h, in air in a programmable furnace with a cooling/heating rate of 5 ºC/min. Then, the color of compound turns into the gray and after is mixed in grinding machine for 2h. The second calcination is performed at 800 ºC for about 24 h at the same cooling/heating rate. For the last formation, the color of powder turns into black and mixed in the grinding machine for 2h to achieve increasingly homogeneity.

3.1.3 Presing and Sintering

The powders are sintered three times, first at 835 ºC for 24 h, second at 840 ºC for 48 h and third at 840 ºC for 48 h in air with a heating and cooling rate of 5 ºC/min. Further, the powder is pressed in rectangular bars with dimensions of 10x4x2 mm^3 by applying a load of 200 MPa at the 300 K before for each three-sintering process. After the first sintering, the bulk is pressed under two steel plates by applying 100 MPa and then the obtained powder is mixed for 2 h by using Si mortar to attain a homogenous mixture. The powder is pelletized using a rectangular bar of 10x4x2 mm^3 under a force of 200 MPa and then is sintered (annealed) at 840 °C for 48 h. After the second sintering, the bulk samples are pulverized for 5 min in an agate mortar and then pelletized by using the same force. Finally, the third sintering process is carried out to give the superconducting phase to the Bi-2223 materials. Further, the preparation method of the Bi-2223 compounds is schematically showed in Figure 3.1.

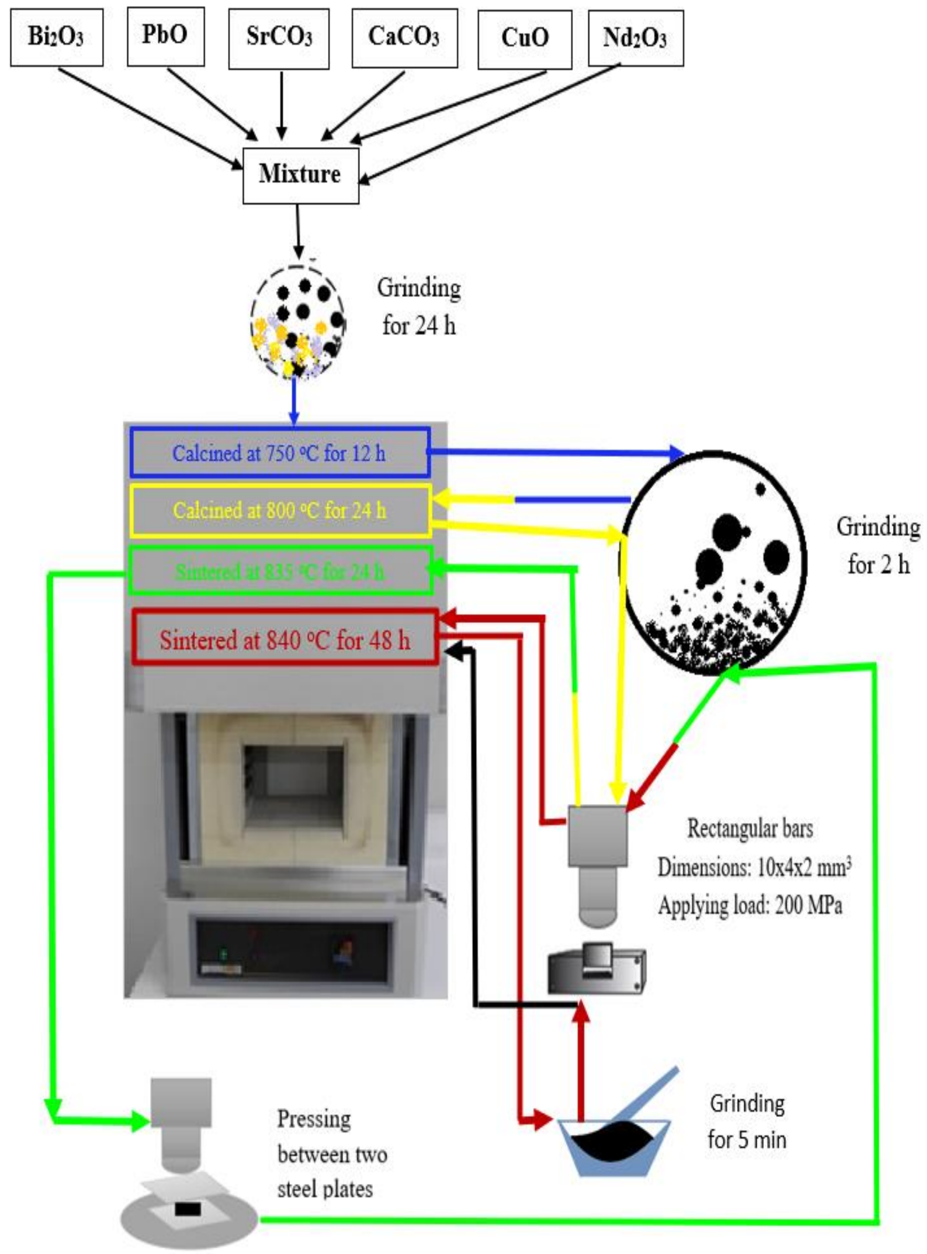

Figure 3.1. The preparation method of the bulk produced in this study.

3.2 X- Ray Diffraction Analysis

X-ray diffraction analysis is a technique used to identify phase investigation, cell size, lattice parameters and texture after different steps of the heat treatment. X-ray diffraction (XRD) data of samples are measured from finely ground powder to obtain regularity. Then, the powder is placed on standard sample holders with a glass substrate. At room temperature, scan is made from 3◦ to 60◦ at a scan speed of 3◦/min and a step increment of 0.02◦. Cu Kα radiation (λ = 1.5418 Å) is used for all powder samples.

3.3 Scanning Electron Microscopy and Energy Dispersive X-Ray Analysis

The scanning electron microscope (SEM) method is commonly used to detect the surface morphology of samples with resolution and high magnification. The properties required in SEM analysis are orientation of grains, change in particle morphology, porosity and the amount of secondary phase observed with increment in substituted level. In this study, the surface morphological performances of all the superconducting samples are determined by means of SEM JEOL 6390-LV. It is done accelerating voltage of 20 kV with a resolution power ~ 3 nm and the magnification range changed is 5000X to 20000X. Further, the X-rays can be used to determine and measure different elements. The particle distribution and composition are examined by SEM prepared with an Oxford X-ray micro-probe (EDX).

3.4 Resistivity vs Temperature (ρ-T) Measurement

In this work, the traditional four-probe DC resistance technique is used for the measurement of ρ-T in annealed bulk samples. Using conductive silver paste, four small lines are made on pellets in a linear alignment to minimize contact resistance. At room temperature, pasted pellets are dried for 15 minutes before linking contacts of copper wires by soldering. While the outer two ends belong to the Keithley 220 programmable dc current source, the voltage between the inner two ends is measured using Keithley 2182A programmable nano-voltmeter. The temperature requirement of resistivity of the sample passing 5 mA DC current from the sample in the cryostat is measured.

3.5 Magnetoresistivity Measurement

The magnetoresistivity measurements are conducted by the four point arrangement implemented. All values are obtained from the resistivity versus temperature graph applied field from 0 T to 2.8 T at constant driving current of 5 mA. Magnetic fields applied in the direction of the drive current are generated by the superconducting coil magnet (CRYO Industries). Interfaced with a computer using Labview computer software, GPIB measurement data are automatically recorded.

3.6 Vickers Hardness Measurement

The mechanical characteristic properties of the produced samples are performed by Vickers hardness measurements by way of the SHIMADZU HVM-2 model digital microhardness tester at 300 K in air. The static pressing loads are exerted on the superconducting samples for the loading period of 10 s in the ranging 0.245 - 2.940 N. The indentation of diagonal is measured with the accurateness about ± 0.1 μm. Two measurement diagonals observed on the surface of sample are adjusted with a calibrated microscope. The measurements of diagonal length are performed at various locations on the sample surface to attain sensible mean values for all applied load, in case we cannot found the values of indentation track due to the surface effects. Further, a universal dynamic mechanical tester (UMT - Bruker SYS2) is used for the indentation tests. Indentations are performed to using a Vickers type indenter. The loads are exerted at 1.0, 2.0, 3.0, 4.0, and 5.0 N for 10 s at 300 K.

4. RESULTS AND DISCUSSION

4.1 Dc Electrical Results of Superconducting Materials

The influence of Sr site Nd impurities on Bi–2223 systemss is studied by difference of the dc electrical resistivity as a function of temperature and the results found are demonstrated in Figure 4.1. While all samples show superconductor state under the onset critical transition temperature T_c^{onset}, metallic behavior is obtained above T_c^{onset}. The room temperature resistivity reduces with the increase in the Nd impurities as exhibit in Table 4.1, confirming the decrements the hole concentration in the Cu–O plane (27, 28). The offset (T_c^{offset}) and onset (T_c^{onset}) critical temperatures examined are determines from Figure 4.1. While the maximum critical temperature (T_c^{offset}) of the pure sample is 108.4 K, a minimum of 78.81 K is obtained for the Nd5 sample. Both the T_c^{onset} and T_c^{offset} values reduce with increment Nd impurities, verifying crystallinity deterioration, crystal size reduction, variations in lattice vibration increment of porosity and weak connections among the grains (29, 30). Moreover, the Nd additives are damaged superconducting properties in consequence of an increase in the improving of the phases of Bi-2201 and Bi-2212 and a decrease in the phase formation velocity of Bi-2223 (31–33). The ΔT_c values shown in Table 4.1 increase from 8.19 K to 29.93 K with increasing Nd additions, verifying of being of pores and weak connections among the superconducting grains and the deviation of hole concentration [34-36]. Further, it is without any doubt that the gradual increment in the ρ_{300K} value results from the combination of deviation in the itinerant charge carrier concentration and formation of new permanent local structural problems (Table 4.1).

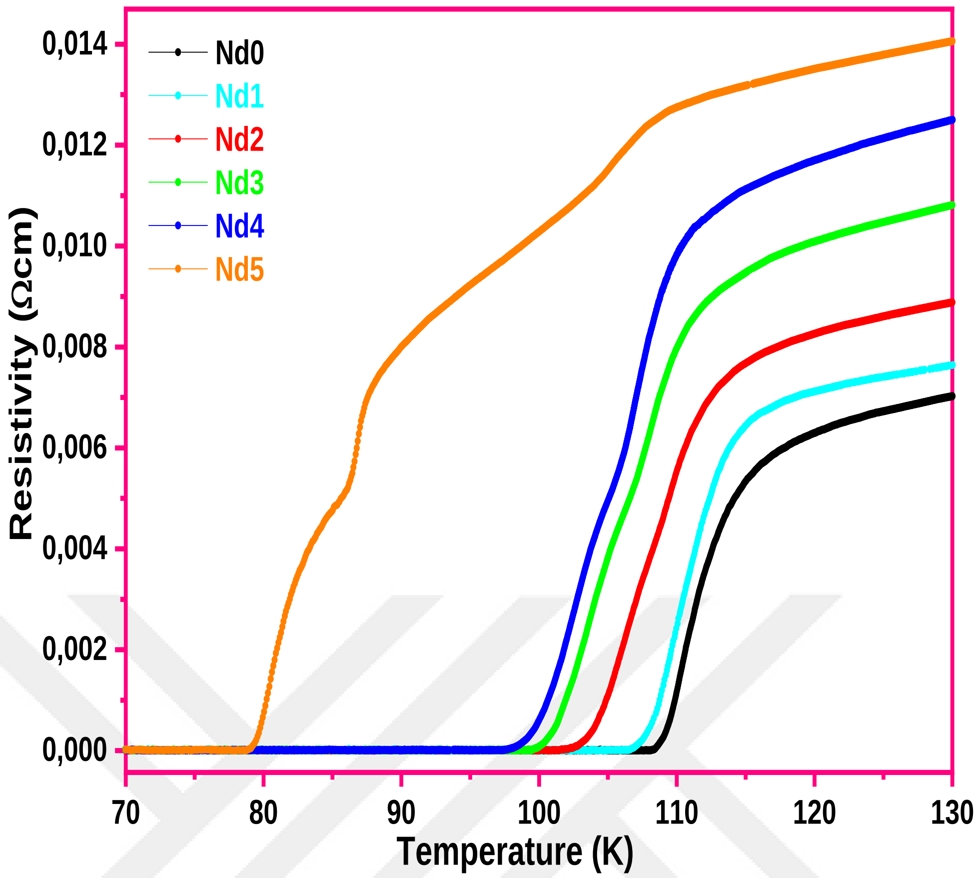

Figure 4.1. Change of dc resistivity for the virgin and Nd substituted-layered Bi-2223 superconducting ceramics.

Table 4.1. Dc resistivity results belonging to the bulk superconductors.

Samples	T_c^{onset} (K)	T_c^{offset} (K)	ΔT_c (K)	ρ_{300K} (Ωcm)
Nd0	116.59	108.4	8.19	0.0140
Nd1	115.80	106.51	9.29	0.0146
Nd2	115.16	101.41	13.75	0.0169
Nd3	110.57	99.45	11.12	0.0190
Nd4	109.98	97.28	12.70	0.0221
Nd5	108.74	78.81	29.93	0.0232

4.2 Powder X-Ray Diffraction Experimental Analyses

The powder x-ray diffraction (XRD) patterns between 3° and 60° are display in Figure 4.2. The peaks of high-T_c Bi-2223, low-T_c Bi-2212 and very low-T_c Bi-2201 phase are demonstrated by Miller indices and are abbreviated by H (*hkl*), L (*hkl*) and VL (*hkl*), respectively. The presence of very low-T_c Bi-2201 for content level x = 0.07 and 0.1, the low-T_c Bi-2212 phases is seen with the Sr site Nd substituted samples, while the high-T_c Bi-2223 and Ca_2PbO_4 is observed for all the samples. With the Nd inclusions in the Cu-O_2 stacked layers, the high- T_c Bi-2223 phase decreases, in fact, the high- T_c Bi-2223 superconductor phase becomes less and less stable. On the other hand, the low-T_c Bi-2212 phases tend to improve with the increasing neodymium concentration level. When the concentration level x = 0.1, the Bi-2212 phase is dominant comparison to Bi-2223 phase. Therefore, the quality of material deteriorates with the increasing Nd additives due to increased structural problems with lattice strains, porosity, voids, defects, grain misorientations, cracks and dislocations. In other way, there is no phases prevent the electron-phonon links to in Cu-O_2 plane. Moreover, the Bi-2212, Bi-2201 and Ca_2PbO_4 phases display low intensity peaks while the high peaks are seen for the Bi-2223 phase (37). The percentages of phase containing Bi-2223, Bi-2212, Bi-2201 and purity (Ca_2PbO_4) are obtained by the following formula, respectively.

$$f_{2223} = \frac{\Sigma I_{2223(hkl)}}{\Sigma I_{2223(hkl)}+\Sigma I_{2212(hkl)}+\Sigma I_{2201(hkl)}+\Sigma I_{Ca_2PbO_4(hkl)}} x100\% \quad (4.1)$$

$$f_{2212} = \frac{\Sigma I_{2212(hkl)}}{\Sigma I_{2223(hkl)}+\Sigma I_{2212(hkl)}+\Sigma I_{2201(hkl)}+\Sigma I_{Ca_2PbO_4(hkl)}} x100\% \quad (4.2)$$

$$f_{2201} = \frac{\Sigma I_{2201(hkl)}}{\Sigma I_{2223(hkl)}+\Sigma I_{2212(hkl)}+\Sigma I_{2201(hkl)}+\Sigma I_{Ca_2PbO_4(hkl)}} x100\% \quad (4.3)$$

$$f_{Ca_2PbO_4} = \frac{\Sigma I_{Ca_2PbO_4(hkl)}}{\Sigma I_{2223(hkl)}+\Sigma I_{2212(hkl)}+\Sigma I_{2201(hkl)}+\Sigma I_{Ca_2PbO_4(hkl)}} x100\% \quad (4.4)$$

where *I* shows the peak intensity. Every calculation is gathered in Table 4.2. From the Table 4.2, the volume fraction of the high-T_c Bi-2223 is 97.55 % for the pure sample. Moreover, the high-T_c Bi-2223 phase decrease from the volume fraction value of 94.43% in Nd1 sample to 26.65% in the Nd impurities level of x=0.1. While the volume fraction belonging to the low-T_c Bi-2212 for the pure sample is zero, the volume fraction increases with the Nd contribution increased and it is found 66.91% for Nd5. Further, at level x = 0.07, the volume fraction of very low- T_c Bi-2201 found as 1.25%, while 2.72% is obtained for the Nd5 sample. After all, amount of Nd participation effects on the formation and reaction of superconducting phases. The H (*002*) peak disappears for the Nd5, while the L (*002*) peak begins to appear for Nd4 and Nd5 samples. Similarly, the peak identified as H (*0010*), H (*113*), H (*1111*) and H (*0012*) not appear for the Nd5. Meanwhile, *a* and *b* lattice parameters for the tetragonal unit cell structure are determined using the $\frac{1}{d^2} = \left(\frac{h^2}{a^2} + \frac{k^2}{b^2} + \frac{l^2}{c^2}\right)$ relationship by diffraction (*hkl*) planes and lattice spacing (*d*) values. From Table 4.3, when the lattice length *c* is determined to be about 37.079 Å for the Nd0 sample, *a* lattice cell is attained to be about 5.402 Å. As the lattice constant *a* increases, the lattice constant *c* values reduces with the increase in the Nd additives. In the Cu-O_2 plane, superconductivity is disturbed because of the decrement in the formation of electron-phonon connection and hole carrier concentrations. According to the Scherrer–Warren equation, crystallite size can be subtracted from the XRD patterns by the formula (38–40):

$$t = {}^{0.941\lambda}/_{\beta cos\theta_\beta} \tag{4.5}$$

where, *t* displays thickness, *λ* shows the wavelength and *β* displays the full width at half maximum (FWHM) and Θ_B is the Bragg angle. Besides,

$$\beta^2 = \beta_m^2 - \beta_s^2 \tag{4.6}$$

where β_s demonstrate the half width in radians. The crystallite size reduces with increasing the Nd nanoparticles (Table 4.3). In addition, we determine the variation of hole carrier concentrations with the Nd content level with the formula (41, 42):

$$P = 0.16 - \left[\frac{\left(1-\frac{T_c^{offset}}{T_c^{Max}}\right)}{82.6}\right]^{1/2} \tag{4.7}$$

in the equation, when the T_c^{offset} values are subtracted from Table 4.1, T_c^{max} is 110 K for Bi-2223. All values are listed in Table 4.3. The pure sample concentration is obtained to be larger than others (Table 4.3), approving that the superconducting properties decrease with the increasing of Nd nanoparticles.

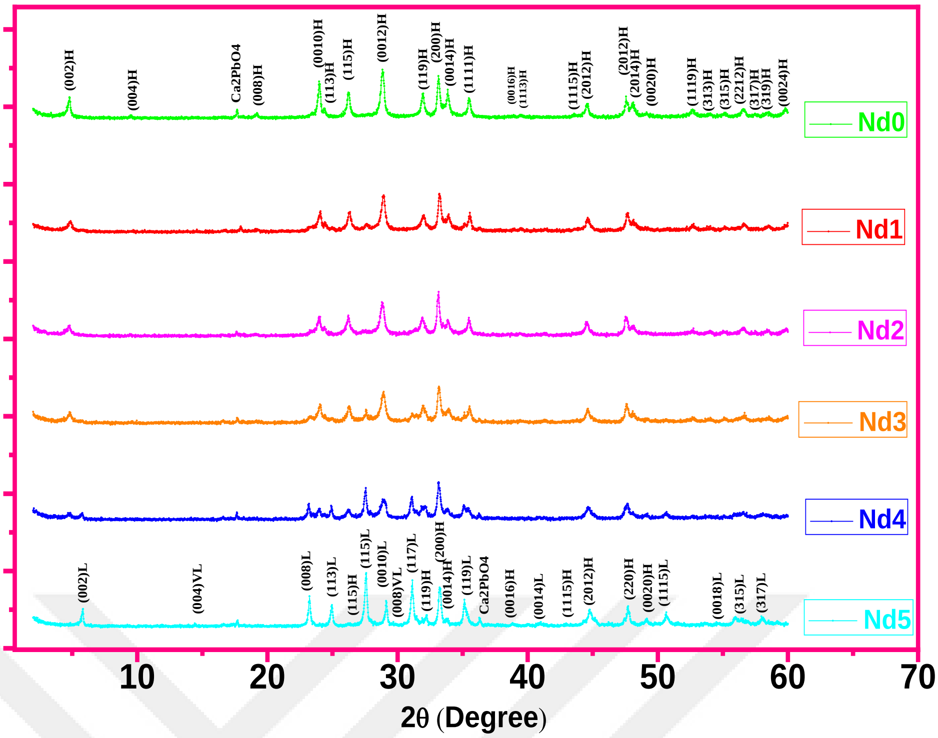

Figure 4.2. Powder X-ray diffraction pattern for pure and Nd/Sr partial replacement of superconducting samples.

Table 4.2. Volume fractions of every sample.

Samples	Volume Fraction (≈%)			
	Bi-2223	Bi-2212	Bi-2201	Ca_2PbO_4
Nd0	97.55	0	0	2.45
Nd1	94.43	3.34	0	2.23
Nd2	94.07	4.10	0	1.83
Nd3	87.73	8.90	0	3.37
Nd4	58.55	34.95	1.25	5.25
Nd5	26.65	66.91	2.72	3.72

Table 4.3. XRD and hole carrier concentrations measurement results for every sample.

Samples	a (Å)	c (Å)	Crystallite size (nm)	P
Nd0	5.402	37.079	59.6	0.146730
Nd1	5.411	36.999	56.3	0.140401
Nd2	5.415	36.973	52.8	0.129252
Nd3	5.429	36.932	49.6	0.125925
Nd4	5.431	36.824	47.5	0.122584
Nd5	5.440	35.385	43.1	0.101410

4.3 Investigation of SEM Images

We examine the scanning electron microscopy (SEM) pictures of Sr site Nd substituted in Bi-2223 materials to analyse the effect of additional mechanisms on the crystallinity and surface morphology at 20000X magnification. Micrographs are demonstrated the differentiation based on texturing (grain alignment distributions and orientations), structural problems (partial melting, voids, defects, and cracks), intragrain problems and inter-grain boundary connection problems obtained on the interaction between the superconducting grains in Figure 4. 3 (43–45). From the Figure 4. 3., the surface morphology view and crystallinity quality are detected to deteriorate with enhancing the Nd purity. Additionally, each sample has a grainy crystalline structure with random alignment distribution and orientation of the grains. Likewise, the basic appearance of the crystal structure is separated from the flaky layers of platelet-like shape with the enhance in Nd purity. In this respect, the pure sample has well connected flaky layers, and thus displays the most uniform surface appearance with the lowest porous (smoothest and densest) structure. On this basis, the images show that the un-substituted material founds the clearest flaky layers of platelet-like structure, largest average grain size distribution and finest connection between the superconducting grains. Further, it is obvious from the figures that a deterioration in uniform surface appearance as a result of structural problems, misorientations of grains and systematic problems in the grain boundary couplings with the increment Nd addition. In this regard, thee

Nd5 sample with distorted crystal structure and purity residues finds the worst SEM picture. That is precisely why, the Nd substitution is not a useful method to provide the surface morphology view and crystallinity quality of Bi-2223 superconducting material.

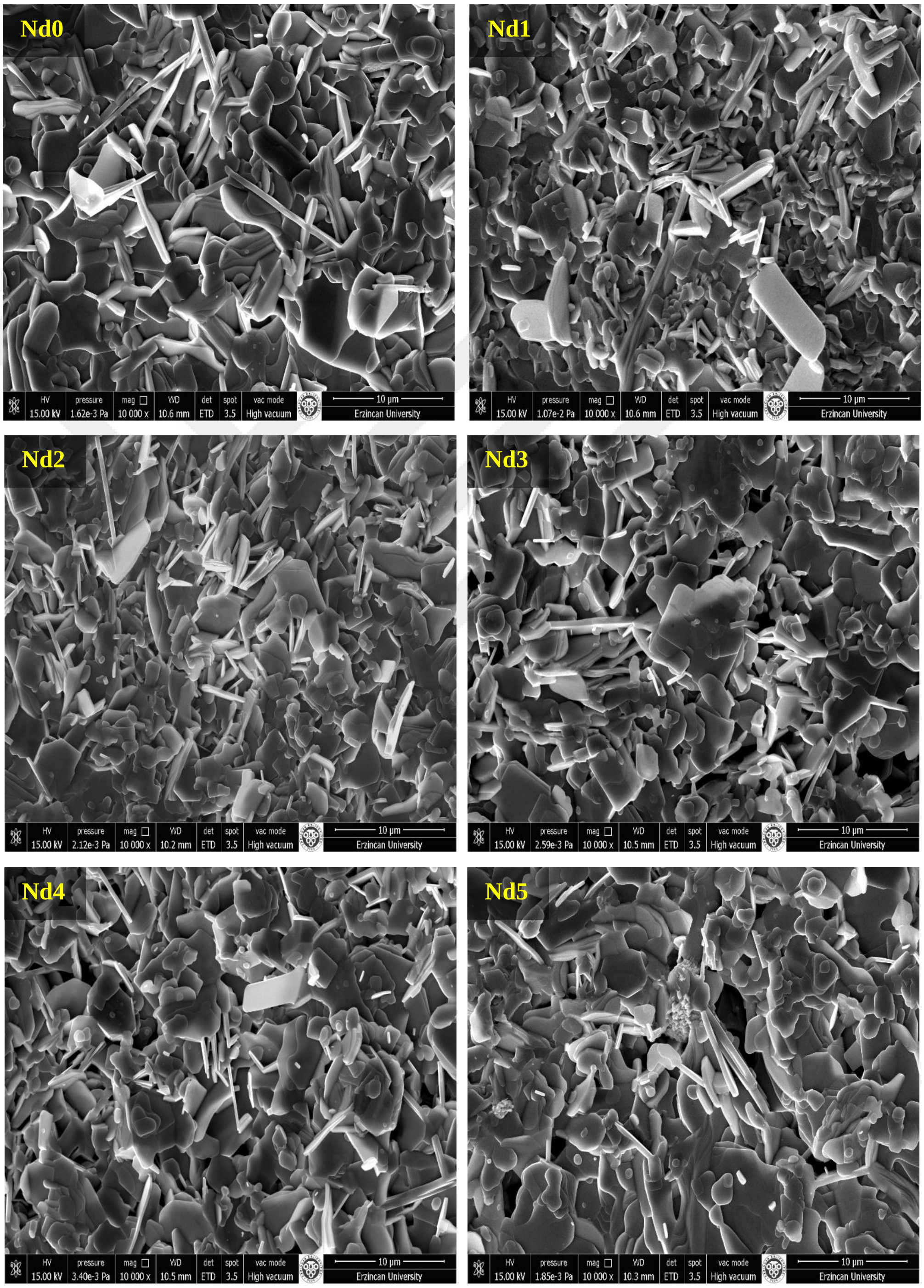

Figure 4.3. SEM micrographs belonging to every sample.

4.4 Analysis of EDX Results

This part (interested in the experimental results of electron dispersive X-ray (EDX) measurements) of thesis enables us to confirm the fact that the aliovalent Nd-sites (Nd+3) mostly replace successfully for the Sr-sites (Sr2+) in the Bi-2223 superconducting matrix. In this regard, the EDX measurements provide quantitatively the distributions of local elemental compositions (Bi, Pb, Sr, Nd, Cu, Ca and O) in Bi-2223 cuprate-layered perovskite superconducting materials prepared. One can see numerically the distributions of local elemental compositions in Table 4.4. It is clear from the table that every material studied contains the used elements (O, Pb, Ca, Sr, Cu, Nd and Bi) as expected. It is, of course, that there is not any clue for the distribution of Nd atoms for the un-substituted material. In other words, neither the extra element distribution (except for the Nd element) nor impurity phases belonging to any anion or cation displays the introduction of every element (O, Pb, Ca, Sr, Cu, Nd and Bi) into the Bi-2223 superconducting system. According to the Figure 4.4, all the peaks obtained are invariant for the pure and Sr-site Nd replaced Bi-2223 superconducting samples and no clue is for the formation of any new phase or compound. The Nd atoms take their position in the interstitial. This is related to the fact that the pure and Sr-site Nd substituted Bi-2223 ceramic materials are perfectly prepared thoroughly (46–48). Additionally, the results in Table 4.4 show that all the elements (except for Nd one) are found to change randomly in the superconducting samples. The local composition distribution of Bi atom is about 28-32% levels as against the value of oxygen atom is about 16-17% while the Pb level is measured to be between about 2-4% for the superconducting compounds. Likewise, the local composition distribution values for the Cu and Ca atoms are obtained to be at about 22-25% and 8-13% levels, respectively. The table also shows slight differences in the distribution of Sr composition. As for the atomic distribution of Nd, it is noticed that the composition level increases systematically as expected. Therefore, it should be emphasized here that deviations occur for some chemical contents in the aliovalent Nd / Sr partially substituted Bi-2223 superconductors. Particularly for the Nd5 sample, the copper deficit increases significantly. In this respect, the composition deviations arise from the compensation of Nd gain in the Bi-2223 ceramics. In short, the variation mentioned above causes drift in the distribution of element concentrations. In addition, the gathering of some atoms over the grain boundaries may causes the small composition deviations in the crystal structure. Based on this result, the change in the composition distributions of Nd and Cu atoms in the Bi-2223 system may be a strong clue for the negative effect of substitution mechanism on the characteristic electrical, superconducting, crystallinity and structural morphology features.

We also analyze the element distribution mappings for every compound in Figure 4.5 to scrutinize whether the elements (Bi, Pb, Sr, Nd, Ca, Cu and O) used distribute homogeneously on the sample surface areas scanned. From the figures, all samples show the uniformly distribution of elements (expect for the neodymium and copper atoms) with the entire area. Furthermore, it is observed that the dots representing copper element compositions are deteriorated, while the dots for neodymium element compositions increased with an increase in the level of Nd impurity. In this regard, the Cu dots reach to the maximum number value as the Nd/Sr substitution level equals to x=0.07. This may be accordance with the fact that the excess Nd atoms start to penetrate over the inter-granular regions in the crystal structure. Hence, it is concluded that the existence of Nd nanoparticles in the crystal structure harms the use of Bi-2223 superconducting materials.

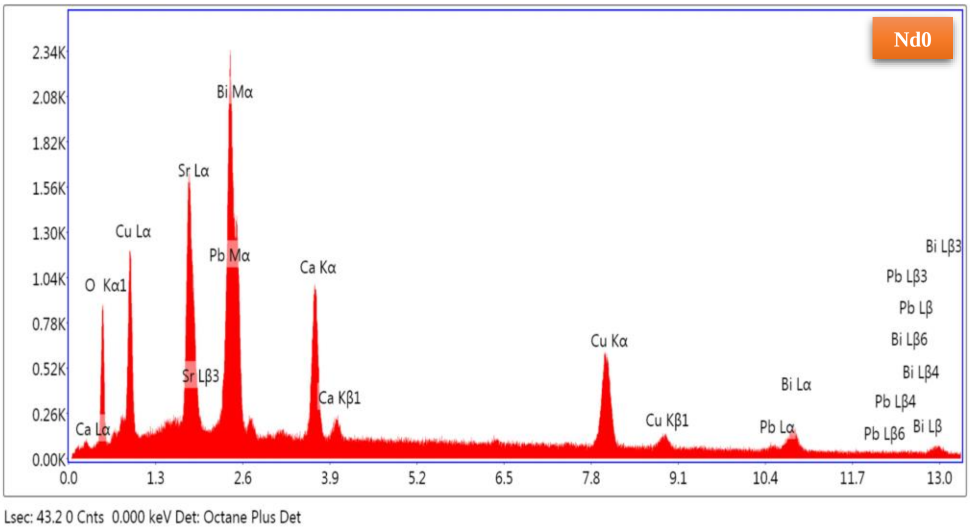
Nd0
Bi Mα
Sr Lα
Cu Lα
Pb Mα
Ca Kα
O Kα1
Sr Lβ3
Ca Kβ1
Ca Lα
Cu Kα
Cu Kβ1
Bi Lα
Pb Lα
Bi Lβ3
Pb Lβ3
Pb Lβ
Bi Lβ6
Bi Lβ4
Pb Lβ4
Pb Lβ6
Bi Lβ
2.34K
2.08K
1.82K
1.56K
1.30K
1.04K
0.78K
0.52K
0.26K
0.00K
0.0
1.3
2.6
3.9
5.2
6.5
7.8
9.1
10.4
11.7
13.0
Lsec: 43.2 0 Cnts 0.000 keV Det: Octane Plus Det

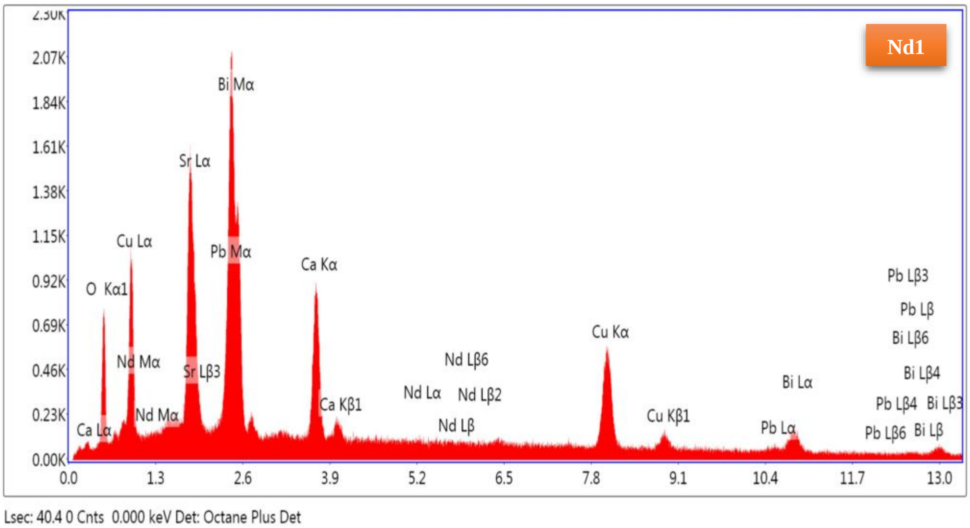
Nd1
Bi Mα
Sr Lα
Cu Lα
Pb Mα
Ca Kα
O Kα1
Nd Mα
Sr Lβ3
Ca Kβ1
Ca Lα
Nd Lβ6
Nd Lα
Nd Lβ2
Nd Lβ
Cu Kα
Cu Kβ1
Bi Lα
Pb Lα
Pb Lβ3
Pb Lβ
Bi Lβ6
Bi Lβ4
Pb Lβ4
Bi Lβ3
Pb Lβ6
Bi Lβ
2.30K
2.07K
1.84K
1.61K
1.38K
1.15K
0.92K
0.69K
0.46K
0.23K
0.00K
0.0
1.3
2.6
3.9
5.2
6.5
7.8
9.1
10.4
11.7
13.0
Lsec: 40.4 0 Cnts 0.000 keV Det: Octane Plus Det

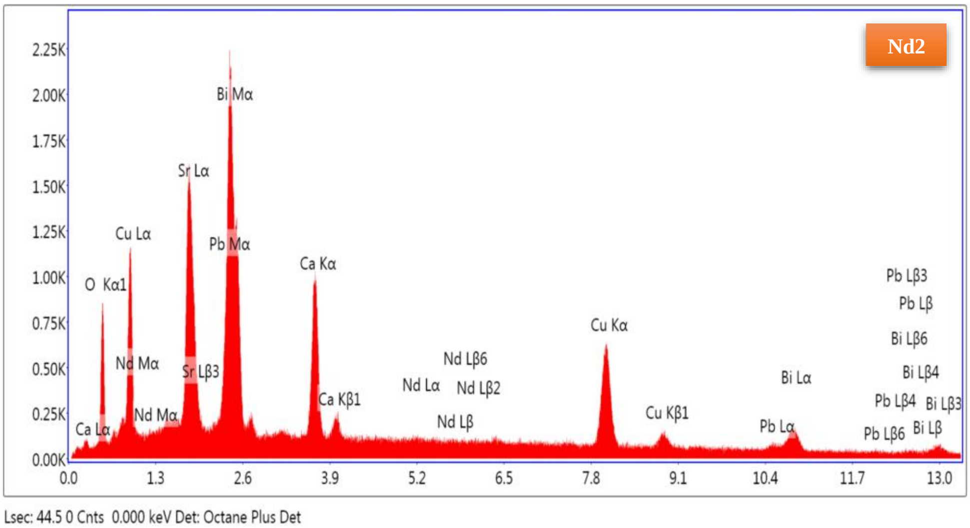
Nd2
Bi Mα
Sr Lα
Cu Lα
Pb Mα
Ca Kα
O Kα1
Nd Mα
Sr Lβ3
Ca Kβ1
Ca Lα
Nd Lβ6
Nd Lα
Nd Lβ2
Nd Lβ
Cu Kα
Cu Kβ1
Bi Lα
Pb Lα
Pb Lβ3
Pb Lβ
Bi Lβ6
Bi Lβ4
Pb Lβ4
Bi Lβ3
Pb Lβ6
Bi Lβ
2.25K
2.00K
1.75K
1.50K
1.25K
1.00K
0.75K
0.50K
0.25K
0.00K
0.0
1.3
2.6
3.9
5.2
6.5
7.8
9.1
10.4
11.7
13.0
Lsec: 44.5 0 Cnts 0.000 keV Det: Octane Plus Det

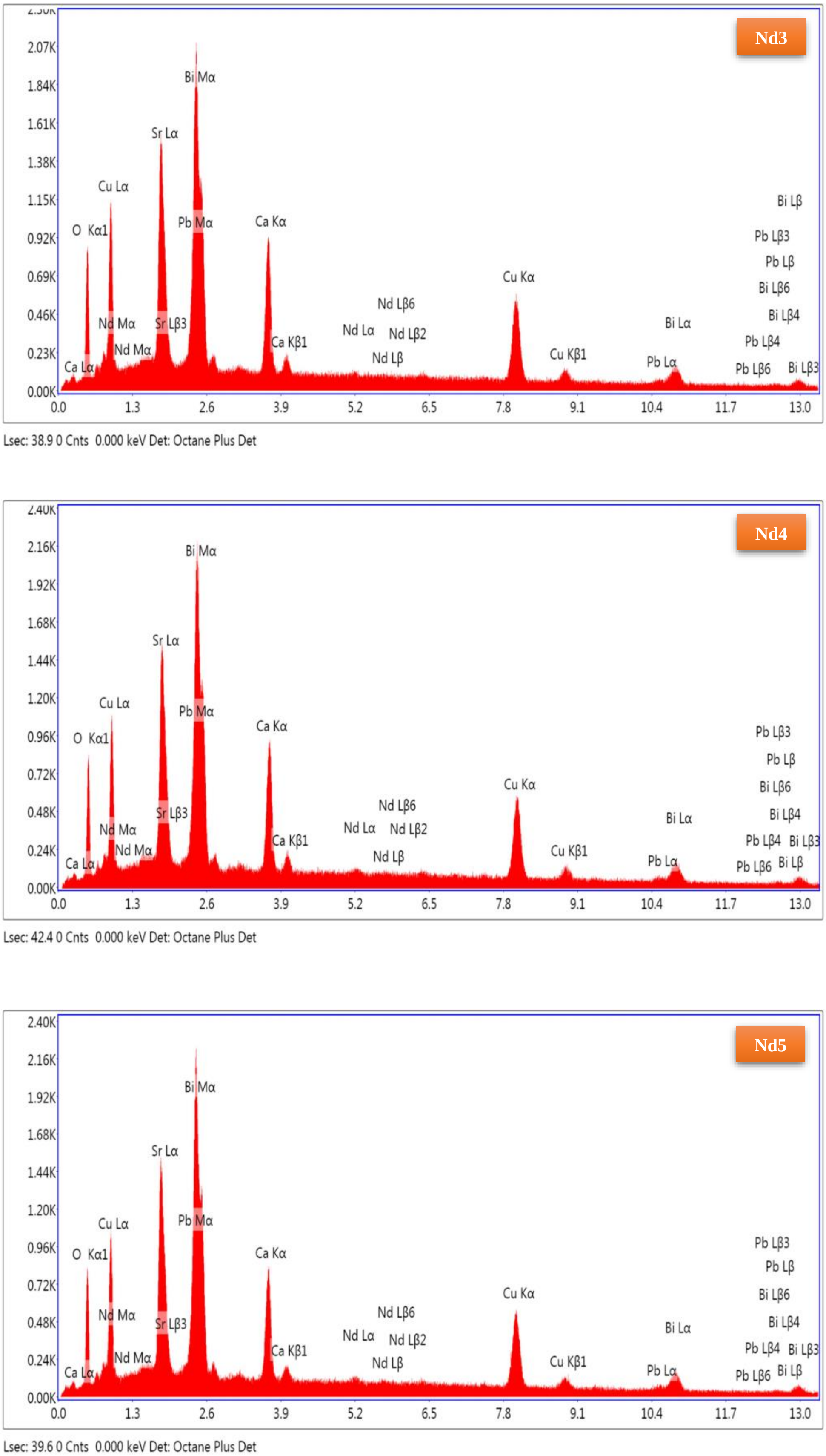

Figure 4.4. EDX Spectroscopy investigation for all samples.

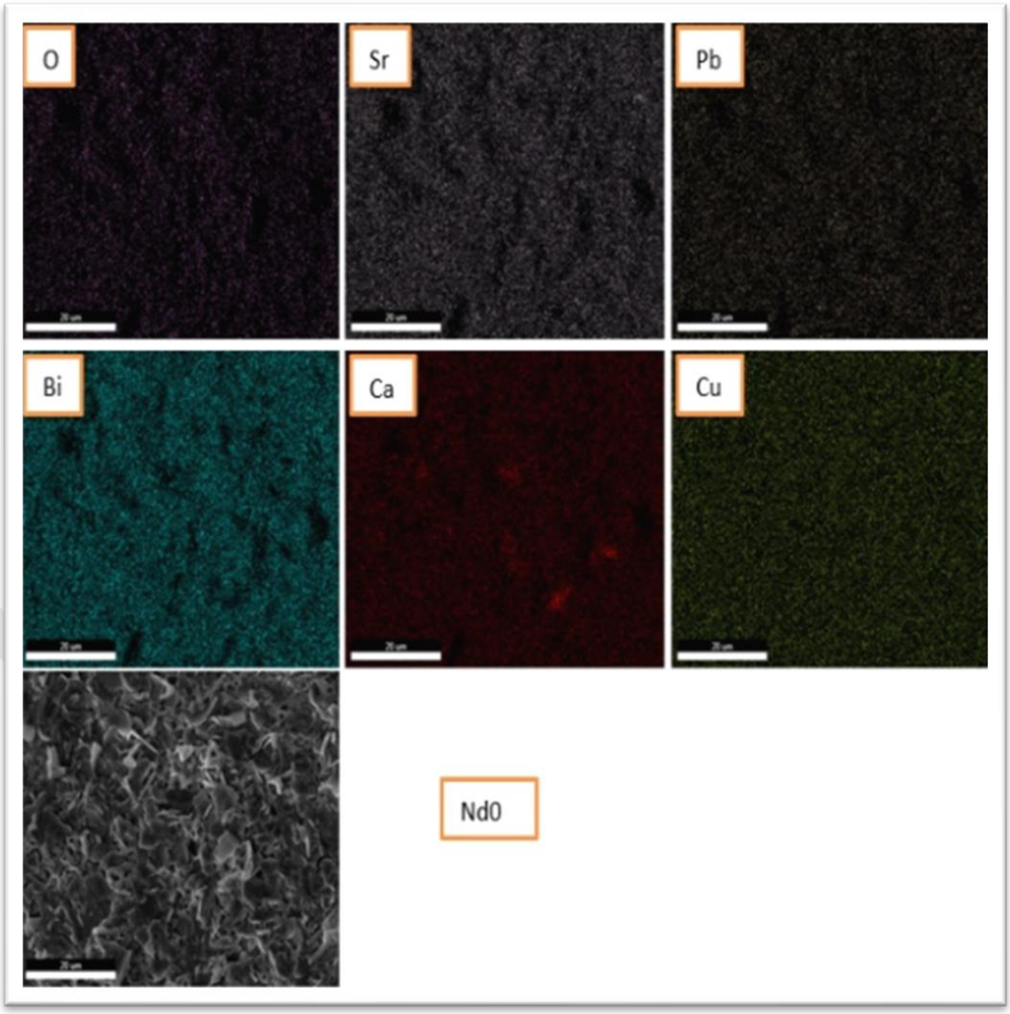

(a)

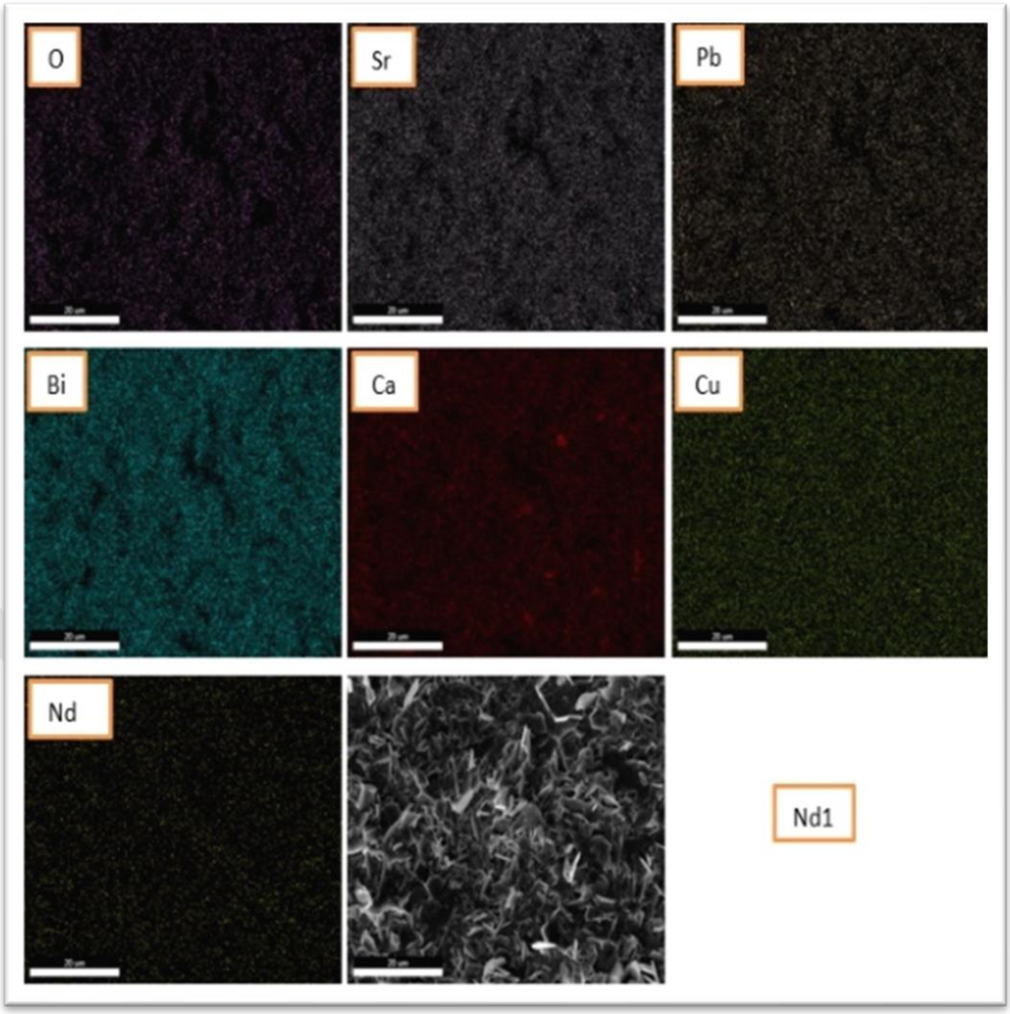

(b)

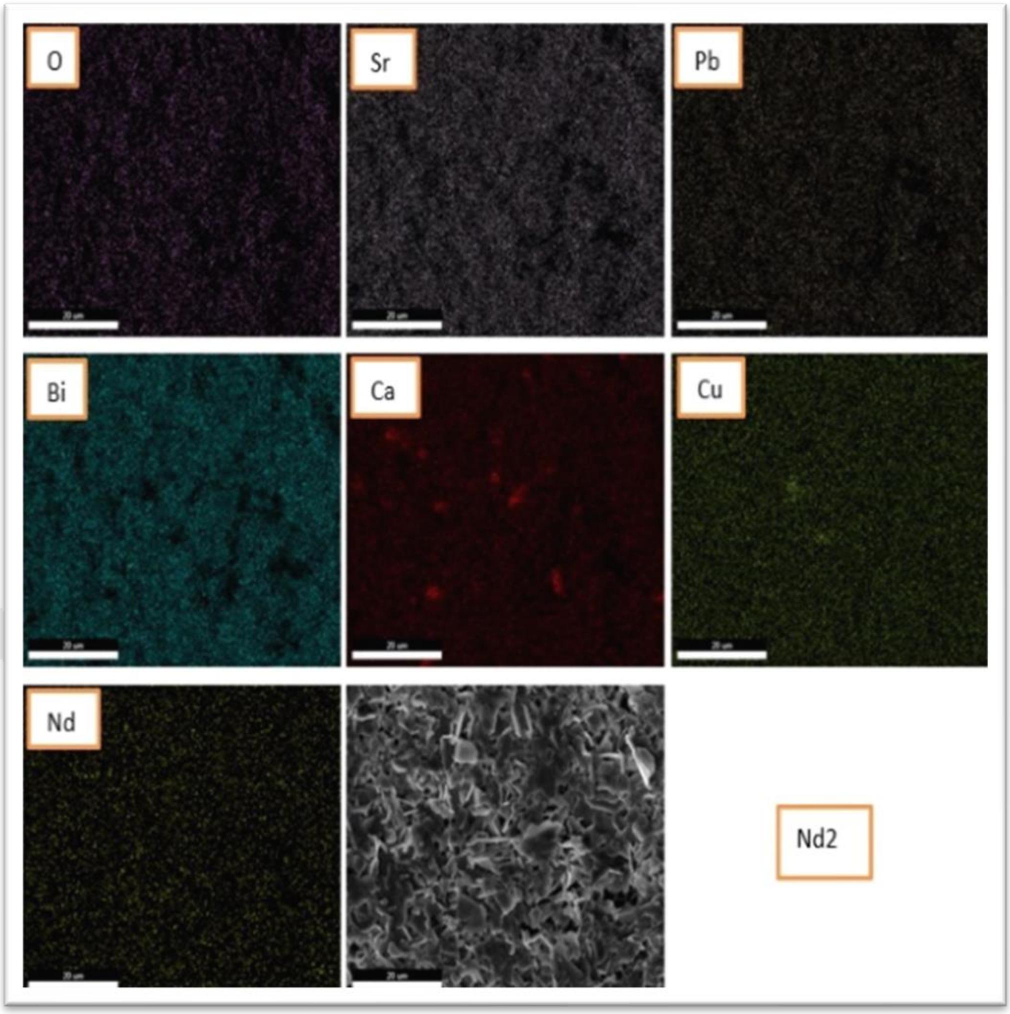

(c)

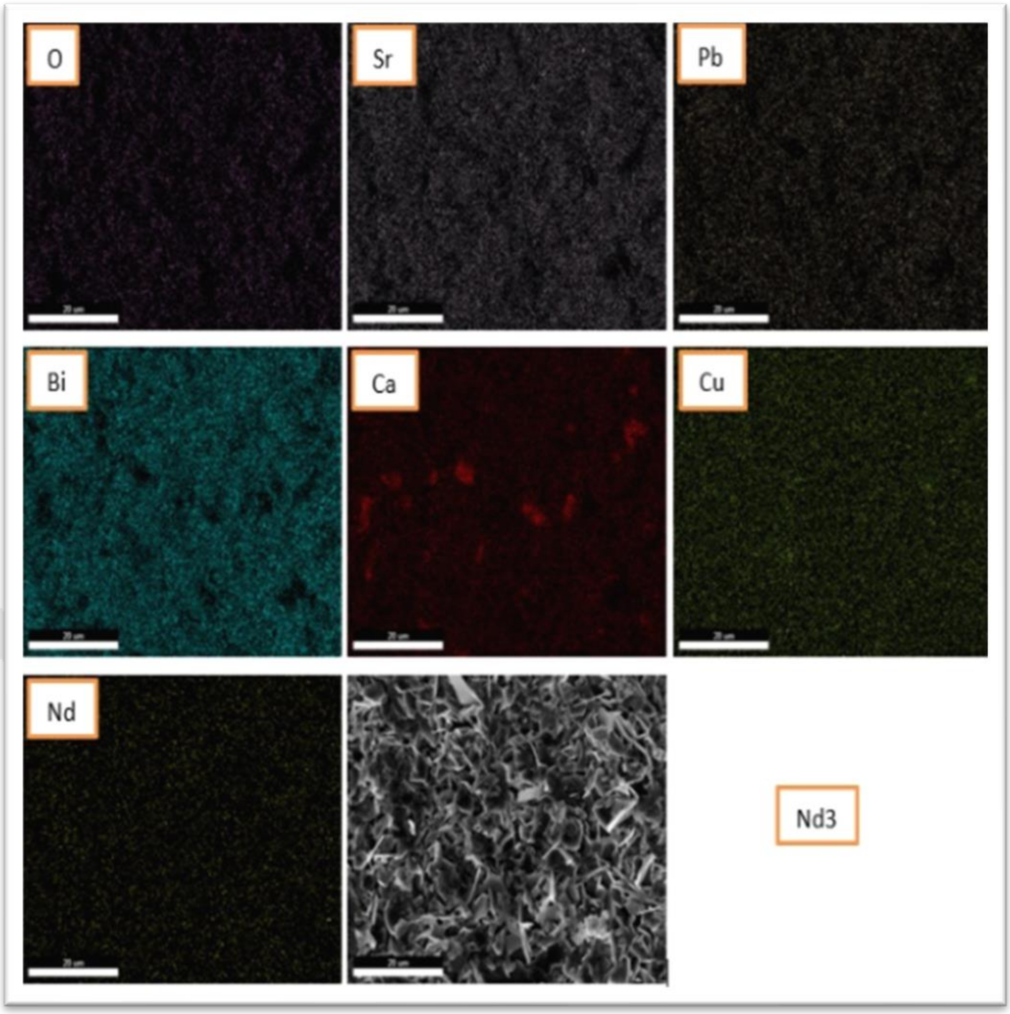

(d)

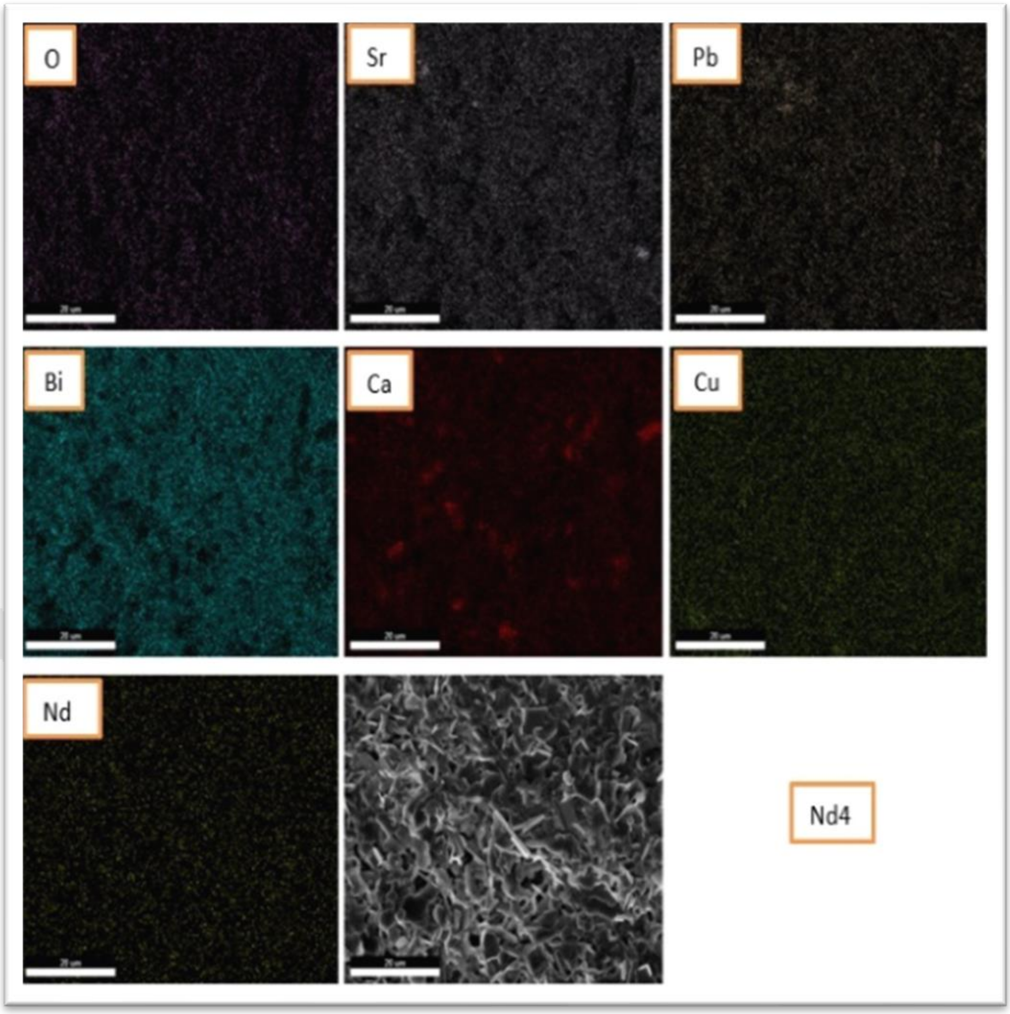

(e)

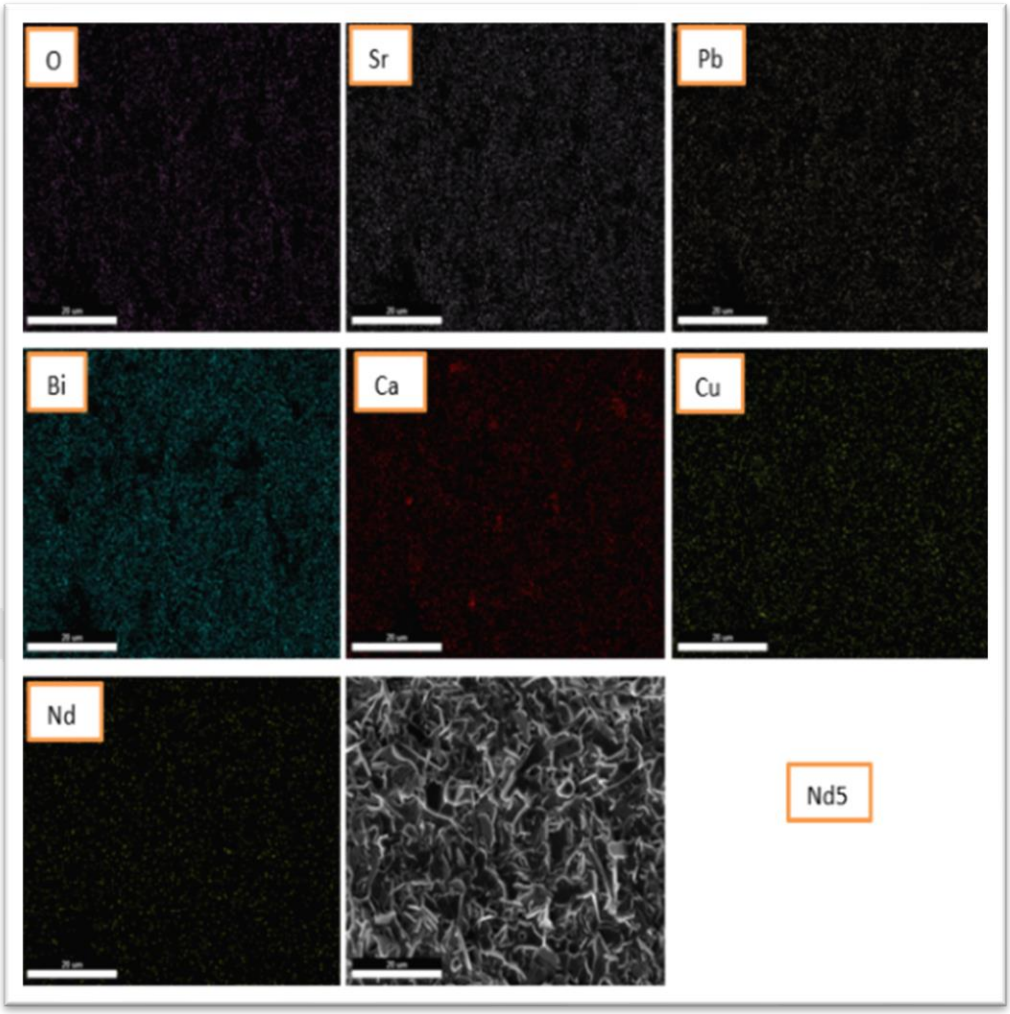

(f)

Figure 4.5. Results of EDX measurements of every sample (a-f).

Table 4.4. Concentrations of the elements in the samples.

Component	Line	Distribution Content (wt.%)					
		Nd0	**Nd1**	**Nd2**	**Nd3**	**Nd4**	**Nd5**
O	Kα	16.99	16.43	16.33	17.75	16.72	16.87
Sr	Lα	14.32	15.84	15.32	15.45	15.12	15.41
Pb	Lα	3.25	2.94	3.78	3.22	3.84	3.39
Bi	Lα	28.15	31.14	29.42	29.59	30.57	31.99
Ca	Kα	12.31	9.58	10.10	9.74	9.67	8.62
Nd	Lα	-	0.33	0.65	0.84	1.10	1.30
Cu	Kα	24.98	23.75	24.40	23.42	22.98	22.43

4.5 Magnetoresistivity Experimental Measurement Findings

We investigate the role of Sr site Nd substituted on the magnetoresistivity characteristic properties of Bi-2223 systems via the change of resistivity versus temperature. In Figure 4.6, experimental magnetoresistivity curves can be observed for each sample. The existence of Nd impurities and applied field influence the magnetoresistivity properties as seen from the Figure 4.6. All T_c^{onset} and T_c^{offset} parameters are tabulated in Table 4.5. The T_c^{offset} and T_c^{onset} values reduction with the enhance in Sr site Nd purities in Bi-2223 samples. The T_c^{onset} values decrease from 116.5 to 108.7 K with Nd impurities, while T_c^{offset} values decrease from 108.4 to 78.8 K in the zero magnetic field. Further, the T_c^{offset} value for the virgin sample is obtained to be about 65.3 K under 2.8 T applied magnetic field. An increase of applied field from 0 T to 2.8 T causes decrease temperatures in the critical temperature values. Consequently, the critical temperature is dependent on the applied field (49, 50). The change of ΔT_c (T_c^{onset} - T_c^{offset}) value is another result deduced from the magnetoresistivity curve. The magnetoresistivity curves enlarges to lower temperature with the increase in the applied magnetic field owing to the reduce of the flux trapping ability, confirming the increment of ΔT_c value. Likewise, the magnetic field damages the Josephson connection and vortex lattice, therefore the flux lines jump to neighbour states. This presents that the applied field increases the separate pancakelike performance along the stacked layers of $Cu\text{-}O_2$ (51). Hence, the increasing of Nd addition along with the applied field destructions the flux trapping, consequently the 2D pancake vortices that jump to near states start to move thermally. Consequently, this illustrates a thermal degeneracy described by the thermally activated flux flow (TAFF) approach (52). Finally, the decrease in the T_c^{offset} values with the applied field is about the theory of pair breaking explained by Gorkov and Abrikosov. Based on this theory, the presence of conduction electron spins in the cooper pairs and linking among the magnetic purities with the spin number, causing the difference in the spin states of the electrons. With the above situation, the practical result disrupts copper pairs and superconducting properties is destructed (53). Evidence from increased Nd addition harms copper pair formations established on the phase coherence.

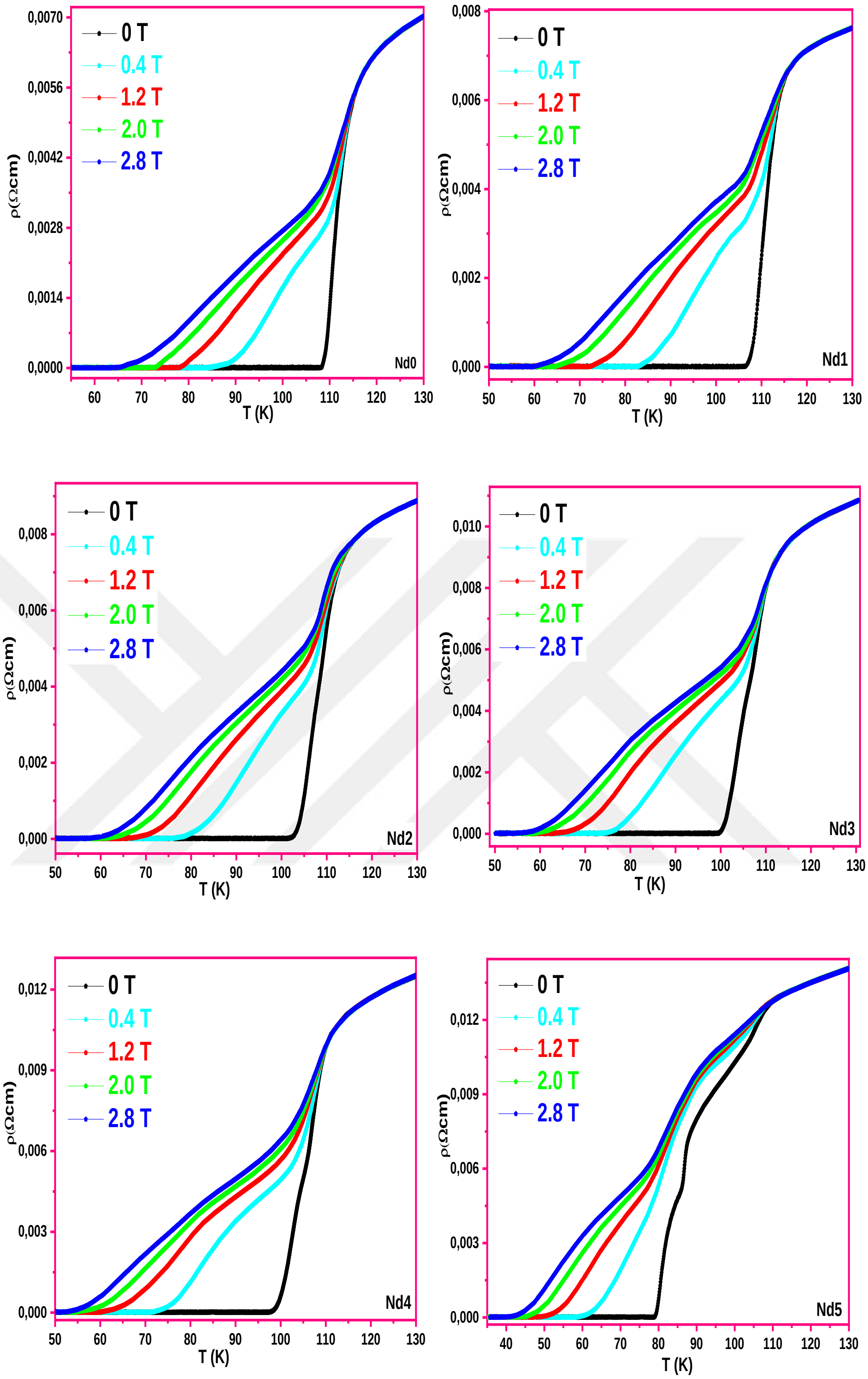

Figure 4.6. ρ-T graphs of the samples at different applied magnetic field.

Table 4.5. T_c^{onset} and T_c^{offset} values of the samples.

Samples	T_c^{onset} (K)	T_c^{offset}(K)				
		0T	**0.4 T**	**1.2 T**	**2.0 T**	**2.8 T**
Nd0	116.5	108.4	85.2	77.9	72.9	65.3
Nd1	115.8	106.5	82.9	72.4	65.5	60.7
Nd2	115.1	102.4	77.9	67.1	61.3	57.4
Nd3	110.5	99.4	74.3	63.6	59.3	55.9
Nd4	109.9	97.6	71.6	59.8	54.3	52.2
Nd5	108.7	78.8	58.4	48.8	45.1	40.2

4.6 Flux Pinning Energy

We analyse the role of Sr-site Nd substituted on the activation energy with the aid the Arrhenius law based on the thermally activated flux flow (TAFF) approach. TAFF model shows both the change of potential energy barriers for the pinning centers and the applied field requirement of effective flux pinning mechanism (54, 55). Besides, the flux pinning (activation) energy are computed from the Arrhenius activation formula:

$$\rho = \rho_0 exp(\frac{U_0}{k_B T}) \tag{4.8}$$

here, U_0 present the activation energy parameter and is attained from the slope of Arrhenius curves, k_B defines to the universal Boltzmann's constant, and the ρ_0 is pre-exponential factor (56). Nonlinear relationships between lnρ/ρ0 versus 1/T graphs in different magnetic fields are given in Figure 4.7. As shown in Table 4.6, the activation energy values reduction with the increment of Nd additives and exterior applied field as result of destruction of the superconductivity. The maximum pinning (activation) energy values for the Nd0 sample is found to be 2351.8 K as against 674.7 K for the Nd5 sample at 0 T. At the 2.8 T, the U_0 values are attained to be about 440.3 K for the Nd0 sample and 122.1 K for Nd5 sample. This ensures that the weak link in the intergranular connection is destroyed, the energy obstructions and the distance among the pinning centers are reduced. Further, all samples show the same feature curves that tend to reduce up to the 0.4 T after that the energies continue to decrement slowly. This confirming is in the attributed to the dispersion of applied magnetic field into only the inter-granular region under 0.4 T exterior field, and the damage of the inter-granular connection in the Cu-O_2 stacked layers (57). Magnetic field dependence of U_0 is obtained by the following power-law formula:

$$U(\mu_0 H) \approx \mu_0 H^{-\beta} \tag{4.9}$$

here, the constant of β illustration the magnetic field influence and the direction of magnetic field. As seen in Table 4.6, the β values are between 0.490 and 0.277. We explained the reduction of β values by the enhancement in the grain border connection problem and limit of weak links. Also, the dependence of β values owing to the Sr site Nd substituted is related to activation energy for the correlated quantized fluxoids based on the level of oxygen content in Bi-O layers, lattice strains defects, dislocations and disorders (58–61).

Table 4.6. Exterior applied field requirement of flux pinning energy.

Samples	**Pinning energies (K)**					**β values**
	0 T	**0.4 T**	**1.2 T**	**2.0 T**	**2.8 T**	
Nd0	2351.8	1186.8	792.2	587.7	440.3	0.490
Nd1	1905.2	950.9	582.3	445.1	420.9	0.435
Nd2	1232.2	710.9	493.2	418.4	383.6	0.320
Nd3	954.3	612.1	448.5	385.9	347.1	0.290
Nd4	901.3	557.3	395.6	327.4	316.8	0.283
Nd5	674.7	216.6	171.5	148.5	122.1	0.277

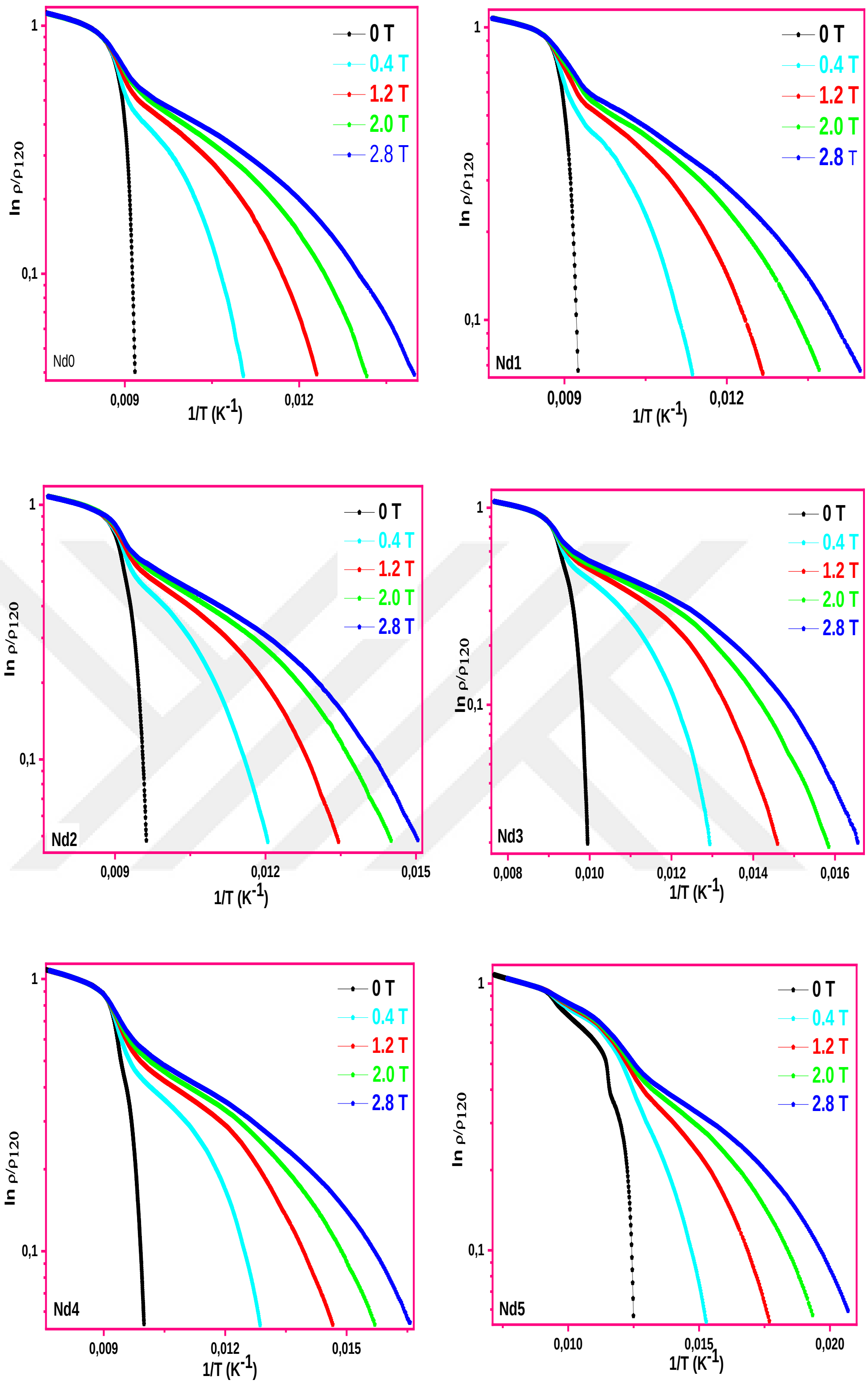

Figure 4.7. Change of lnρ/ρ0 as a function of 1/T graphs of superconducting materials.

4.7 Irreversibility and Upper Critical Field

We carry out the magnetoresistivity measurements under the applied field range of 0 T-2.8 T. As a function of the applied field, the dependence of magnetoresistivity on temperature is provided as given relationships (62, 63).

$$\rho(\mu_0 H_{irr}, T) = 0.1\rho_n \, \mu_0 H_{irr}(T) \tag{4.10}$$

$$\rho(\mu_0 H_{c2}, T) = 0.9\rho_n \, \mu_0 H_{c2}(T) \tag{4.11}$$

where ρ_n exhibitions the normal state resistivity 120 K. After the μ_0H_{irr} (T) and μ_0H_{c2} (T) parameters are defined in the Schubnikov phase, the extrapolation intersections to the zero point provide the values of μ_0H_{irr} (0) and μ_0H_{c2} respectively (64). The irreversibility fields (μ_0H_{irr}) and upper critical fields (μ_0H_{c2}) against temperature change are demonstrated in Figure 4.8 and Figure 4.9, respectively. Theoretically we determine the values of μ_0H_{irr} (0) and μ_0H_{c2}(0) by extrapolation of the curve at 0 K and give the found data in Table 4.7. Computed the μ_0H_{irr} (0) values reduce from 8.29 to 5.81 T; similarly, the μ_0H_{c2} (0) values reduce from 719.58 to 54.23 T with increment of Nd additives, approving destroying the pinning abilities owing to the double breaking mechanism.

Table 4.7. Irreversibility field and upper critical field of the samples.

Samples	μ_0H_{irr} (0) (T)	μ_0H_{c2} (0) (T)
Nd0	8.29	719.58
Nd1	7.37	299.07
Nd2	7.32	216.01
Nd3	6.81	159.06
Nd4	6.32	129.68
Nd5	5.81	54.23

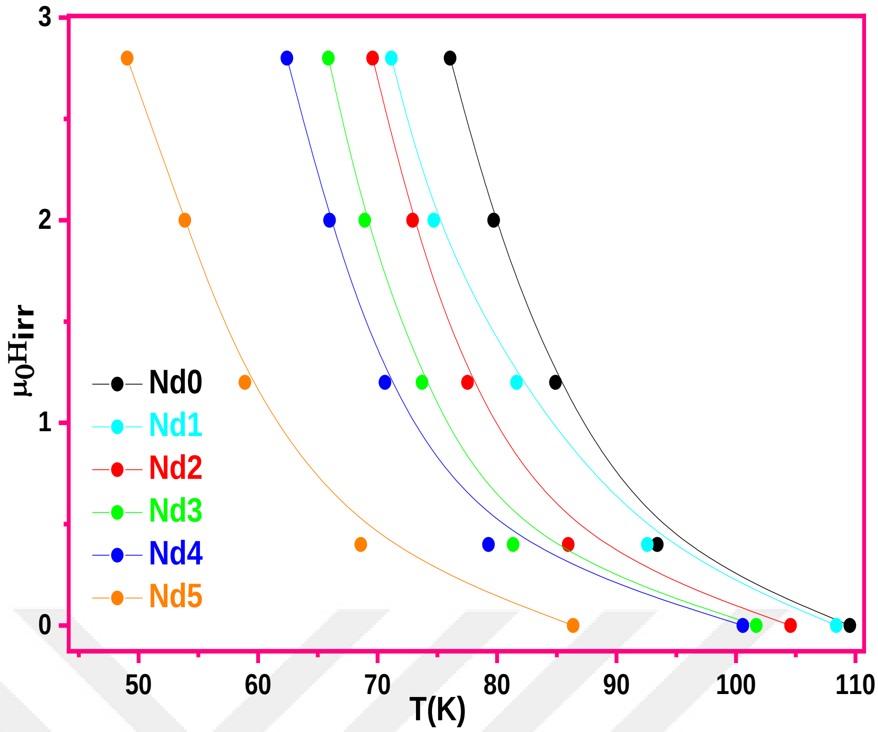

Figure 4.8. The temperature dependences of the irreversibility field.

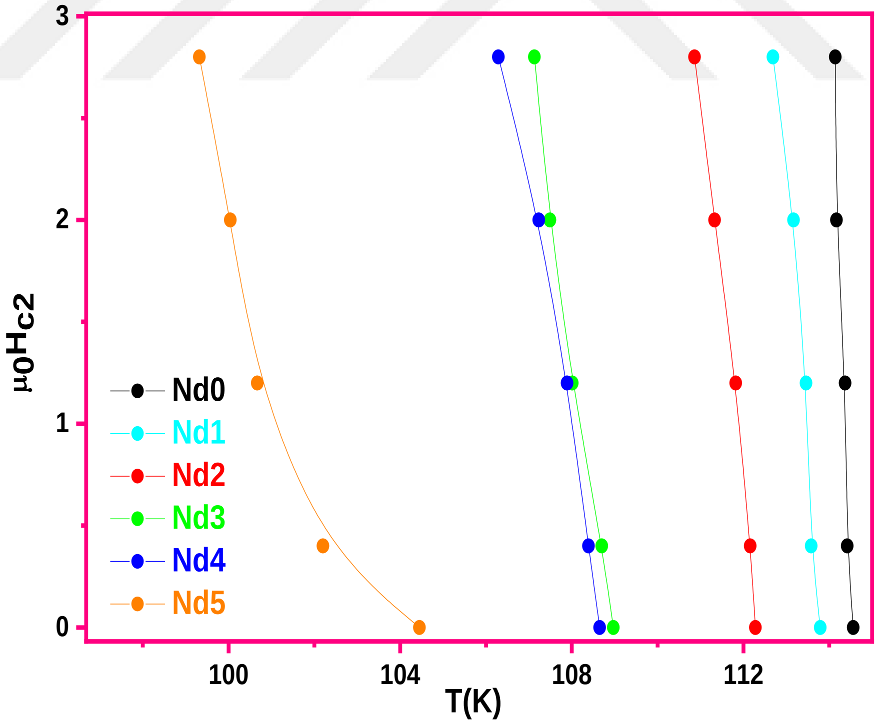

Figure 4.9. The temperature dependences of the upper critical field.

4.8 Coherence Length and Penetration Depth

At 0 K, we can calculate the values of penetration depth (λ) and coherence length (ξ) as the given relationships (65, 66):

$$\lambda(T) = [\frac{\varphi_0}{2\pi\mu_0 H_{c2}(T)}]^{\frac{1}{2}} \quad (4.12)$$

$$\xi(T) = [\frac{\varphi_0}{2\pi\mu_0 H_{irr}(T)}]^{\frac{1}{2}} \quad (4.13)$$

here, φ_0 is equal to 2.07×10^{-15} Tm^2. All the ξ(0) and λ(0) values computed are tabulated in Table 4.8. the coherence lengths increment from 63.04 to 75.30 Å instead, the penetration depths increase from 6.77 to 24.65 Å with the increment in the Nd impurities. This may be related to the fact that the increasing Nd additives the formation of two-dimensional flattened pancake vortices by decreasing the level of energy barrier.

Table 4.8. Coherence length and penetration depth values of the samples.

Samples	**ξ_0 (Å)**	**λ_0 (Å)**
Nd0	63.04	6.77
Nd1	66.86	10.50
Nd2	67.09	12.35
Nd3	69.55	14.39
Nd4	72.20	15.94
Nd5	75.30	24.65

4.9 M-H Measurements

It is found that every superconducting compound prepared presents the large hysteresis loops at the temperature of 77 K. This is attributed to the fact that the pure and Sr-site Nd substituted Bi-2223 ceramic materials (especially the pure one) exhibit good and uniform superconductivity. Besides, it is apparent from the Figure 4.10 that the shapes of M–H curves tend to enlarge with the increment in the Sr/Nd substitution level in the presence of applied filed strengths as a result of the increment in the hysteresis losses. For the pure and low external fields, the loops are look like elliptical shape (anticipated as the grain contribution or penetration of magnetic field into only intra grain regions with small proportion) whereas the Sr/Nd substitution and relatively higher external fields make the shape distort harshly (intra and inter granular regions). In fact, the M–H curves for the Nd5 sample almost are disappeared. The change of the loops can thoroughly be explained by the combination of Bean–Livingstone effect and different viscous effects where the distortion is described by the formation of defects on the specimen surface. Namely, the Bi-2223 superconducting phase firstly begin to form at the surface and the process continues slowly and slowly towards to the core of sample (converting the phases to the main superconducting phase of Bi-2223). Hence, the defects form automatically on the surface (general characteristics of Bi-2223 phase formation) of a sample, and the presence of discrete fluxoids (due to the external magnetic field) leads to change the shape of magnetization curves (67). Besides, the hysteresis loops of materials studied are used to calculate the critical current densities via the Bean model due to the rectangular cylinder shapes of experimental loops. At the same time, the Bean model is superior and simple to find the critical current density value of a superconducting material using the following formula (68):

$$J_c = \frac{20\Delta M}{a(1-\frac{a}{3b})} \tag{4.14}$$

in the equation the constants of a and b are the width and thickness of material studied, respectively. Here b is larger than a. Besides, the abbreviation of $\Delta M = M_+ - M_-$ is in correspondence to the electromagnetism of unit volume. Further, the magnetization values of parameters are related to the zero-field values of different loops at the various maximum fields. The critical current densities (J_c) are obtained to be about $2.17\text{x}10^4$, $1.58\ \text{x}10^4$, $1.49\ \text{x}10^4$, $1.18\ \text{x}10^4$, $0.35\ \text{x}10^4$ and $0.13\ \text{x}10^4$ Acm^{-2} for the Nd0, Nd1, Nd2, Nd3, Nd4 and Nd5 samples, respectively. The J_c value decreases dramatically with the increment in the Sr/Nd substitution level. On this basis, the maximum J_c value of $2.17\text{x}10^4$ A/cm^2 is noted for the pure sample while the Nd5 sample shows the minimum performance for J_c parameter ($0.13\text{x}10^4$ A/cm^2). Similarly, the enhancement in the external magnetic field damages seriously the J_c value. This is directly related to the suppression in not only the flux pinning ability but strength of coupled vortices of Bi-2223 superconducting material due to the random distribution or contraction of distance between the pinning centers. Shortly, the existence of Nd atoms in the Bi-2223 crystal structure degrades the elasticity of vortex lattice. The rapid decrement in the J_c parameters with the entering of Nd ions into the Bi-2223 crystal lattice can also be explained by the differentiation in the crystallite sizes, densification degree, decomposition of

Bi-2223 superconducting phase into the impurity phases (reduction of Bi-2223 phase fraction percentage) and especially interaction between the superconducting grains. Moreover, the diminish in the critical current density parameter with the Sr/Nd substitution in the Bi-2223 crystal system can more phenomenologically and sophisticatedly be discussed as follows: the replacement of trivalent cation Nd3+ for a divalent cation Sr2+ favors the improvement in the decoupling of adjacent layers (recoupling linelike or discrete pancakelike nature) in the Bi-2223 superconducting crystal system. Accordingly, Nd-5 ceramic material exhibits the lowest J_c values at any applied magnetic fields.

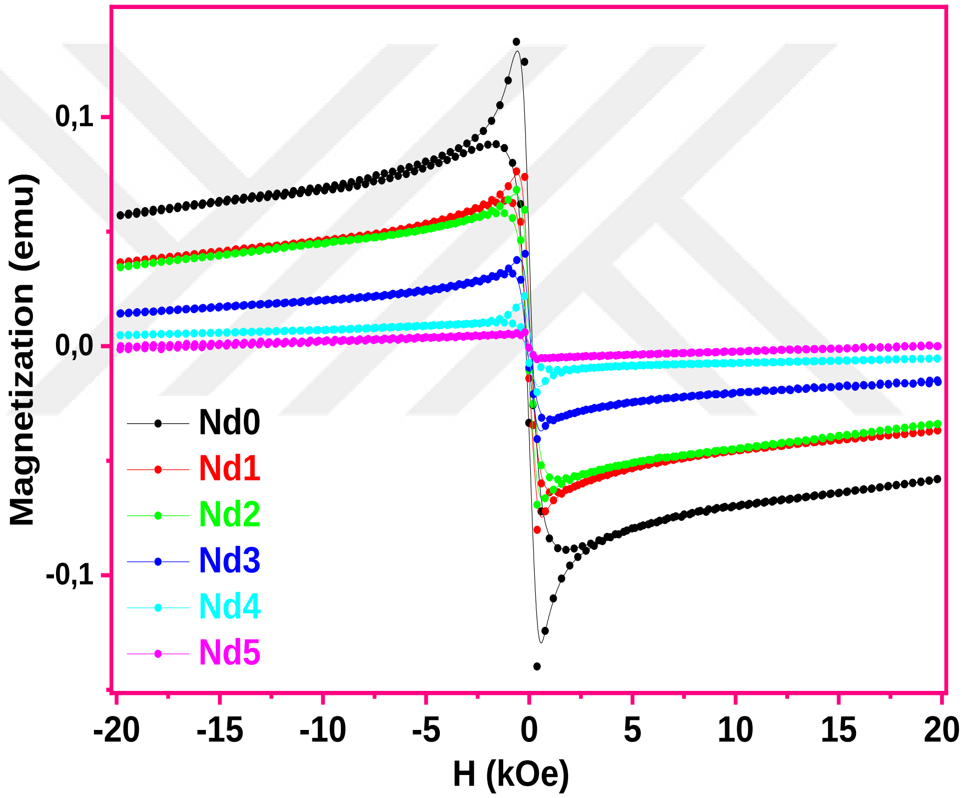

Figure 4.10. Magnetization curves of in samples at 77 K.

4.10 Microhardness Properties Examined by Static Micro-Indentation Technique and Modeling

The Vickers hardness test is used for definition of microhardness values of $Bi_{1.8}Pb_{0.35}Sr_{1,9-y}Nd_yCa_{2.2}Cu_3O_x$ (0.00 ≤ x ≤ 0.10) samples. The load dependent microhardness (H_v) values are determined by experimental values of diagonal length (d). The H_v values of dissimilar applied loads (0.245 N ≤ F ≤ 2.940 N) can be computed using the following 8(69, 70):

$$H_V = 1854.4(\frac{F}{d^2}) \tag{4.15}$$

The H_v values reduce with the increasing content of Nd purity and applied load which can be seen in the load dependent hardness versus the applied load showed in Figure 4.11. Apparently, the indentation size effect (*ISE*) nature is exhibit for the all crystal texturing samples. Additional, decreasing the H_v values with the applied load as shown in the Table 4.9. After F = 2 N, the graphs move to the satiation region. Further, the E (elastic modulus), Y (yield strength), K_{IC} (fracture toughness), B (brittleness index) and C_{11} (elastic stiffness coefficient) parameters are deduced by using the following equations (71):

$$E = 81.9635 H_V \tag{4.16}$$

$$Y \approx \frac{H_V}{3} \tag{4.17}$$

$$K_{IC} = \sqrt{2E\alpha} \quad (\alpha; \text{surface energy}) \tag{4.18}$$

$$B = \frac{H_V}{K_{IC}} \tag{4.19}$$

$$C_{11} = H_v^{7/4} \tag{4.20}$$

The load-dependent characteristic parameters are summarized in Table 4.9. It is visible from the table the E values decreases significantly with the increment in the Nd inclusions. The elastic modulus for Nd5 samples values are obtained to be about 50.001 GPa and 32.443 GPa for static compression load 0.245 N and 2.940 N, respectively. This verifies that the increasing of Nd additivities level deteriorates the stiffness, fracture, mechanical stability, flexural strength and durability. Also, the resistant against the strain or permanent deterioration decrease with increasing Nd content. The Y values are determined from equation 4.17 and statistically summarized in Table 4.9. For the load of 0.245 N, the highest Y value of 0.328 GPa is found for the Nd0 inclusions, while a minimum Y value of 0.211 GPa is attained for the Nd5 sample. This is related to the increment of cracks and induced artificial voids. The fracture toughness values are gathered from equation 4.18 and presented in Table 4.9. The K_{IC} values of Nd0 sample decrement from 0.738 to 0.659 GPa with increasing the applied load. This means that the movement of induced dislocations, cracks and voids because of reduction of crack length reaches quickly to their critical propagation velocities. Incidentally, the C_{11} values are computed by using equation 4.20 and shown in Table 4.9. The elastic stiffness coefficient is observed as 0.972 GPa (maximum value) for the Nd0, while the minimum 0.450 GPa value is related to the Nd5 material under load of 0.25 N. As a result, it is concluded that their durability, stiffness, fracture and flexural strengths are reduced.

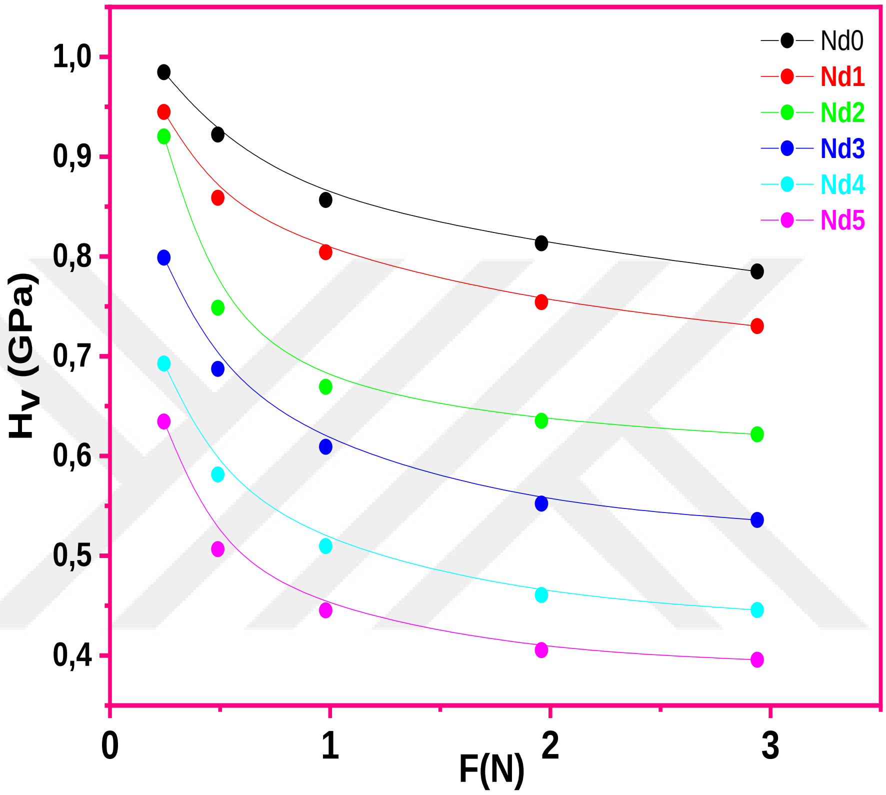

Figure 4.11. Applied load dependence of Vickers hardness.

Table 4.9. H_v, E, Y, K_{IC}, B, C_{11} parameters values for all samples.

Samples	d (μm)	F (N)	H_v (GPa)	E (GPa)	Y (GPa)	K_{Ic} ($Pa/m^{1/2}$)	C_{11} (GPa)	B ($\mu m^{1/2}$)
Nd0	21.48	0.245	0.984	80.708	0.328	0.738	0.972	1.332
	31.39	0.490	0.922	75.585	0.307	0.715	0.867	1.289
	46.06	0.980	0.856	70.210	0.285	0.689	0.761	1.242
	66.86	1.960	0.813	66.641	0.271	0.671	0.696	1.210
	83.34	2.940	0.784	64.337	0.261	0.659	0.653	1.189
Nd1	21.93	0.245	0.944	77.430	0.314	0.740	0.904	1.275
	32.53	0.490	0.858	70.380	0.286	0.706	0.764	1.215
	47.54	0.980	0.804	65.907	0.268	0.683	0.682	1.176
	69.42	1.960	0.754	61.817	0.251	0.661	0.610	1.139
	86.41	2.940	0.730	59.847	0.243	0.651	0.576	1.121
Nd2	22.22	0.245	0.920	75.422	0.306	0.799	0.864	1.151
	34.84	0.490	0.748	61.356	0.249	0.721	0.601	1.038
	52.11	0.980	0.669	54.853	0.223	0.681	0.494	0.981
	75.64	1.960	0.635	52.068	0.211	0.664	0.451	0.956
	93.64	2.940	0.621	50.962	0.207	0.657	0.434	0.946
Nd3	23.85	0.245	0.798	65.465	0.266	0.244	0.673	3.270
	36.36	0.490	0.687	56.334	0.229	0.226	0.518	3.033
	54.62	0.980	0.609	49.928	0.203	0.213	0.419	2.855
	81.13	1.960	0.552	45.260	0.184	0.203	0.353	2.719
	100.87	2.940	0.535	43.918	0.178	0.200	0.334	2.678
Nd4	25.61	0.245	0.692	56.776	0.230	0.713	0.525	0.970
	39.53	0.490	0.581	47.661	0.193	0.653	0.386	0.889
	59.71	0.980	0.509	41.778	0.169	0.612	0.306	0.832
	88.83	1.960	0.460	37.753	0.153	0.581	0.256	0.791
	110.6	2.940	0.445	36.530	0.148	0.572	0.242	0.778
Nd5	26.76	0.245	0.634	52.001	0.211	0.664	0.450	0.954
	42.35	0.490	0.506	41.525	0.168	0.594	0.303	0.852
	63.88	0.980	0.445	36.502	0.148	0.556	0.242	0.799
	94.69	1.960	0.405	33.225	0.135	0.531	0.205	0.762
	117.36	2.940	0.395	32.443	0.131	0.525	0.196	0.753

4.10.1 Meyer's Law

The material shows the ISE or RISE behavior according to the Meyer number (n) values associated with the average indentation diagonal length (d) and load (F). The formula can be seen by following equation (72):

$$F = A_{MEYER} d^n \tag{4.21}$$

The *n* and standard microhardness constants (A_{MEYER}) obtained from the linear *lnF* versus *lnd* (Figure 4.12) graphs are presented in Table 4.10. The slope of the curve gives the Meyer number and A_{MEYER} values are obtained from the intersection points. The *n* values are attained less than 2 (n < 2), confirming the ISE behavior (73).

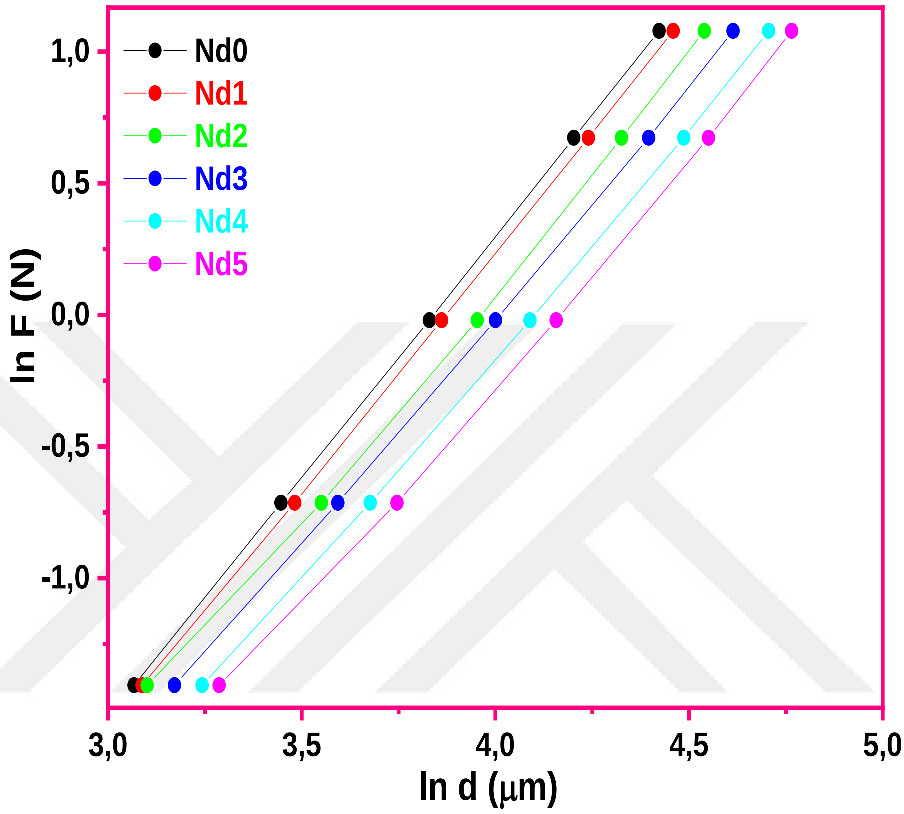

Figure 4.12. ln (*F*) as a function of indentation diagonal length ln (*d*) for all the samples.

Table 4.10. Experimental results values based on Meyer's Law.

Samples	Meyer's law		Hv (GPa)
	A_{MEYER} (N/μm^2)	n	
Nd0	-7.0299	1.832	0.784 – 0.813
Nd1	-7.0214	1.814	0.730 – 0.754
Nd2	-6.8272	1.733	0.621 – 0.635
Nd3	-6.8843	1.721	0.535 – 0.552
Nd4	-6.9373	1.697	0.445 – 0.460
Nd5	-6.9815	1.683	0.395 – 0.405

4.10.2 Analysis of Load Independent Hardness Parameters Based on Proportional Sample Resistance Model

The proportional sample resistance (PSR) model can be identified by way of following formula 4.22. Here, the value of α is the surface energy and second coefficient of β is hardness constant (74).

$$\frac{F}{d} = \alpha + \beta d \tag{4.22}$$

Figure 4.13 show the linear graphs of [F/d–d] for every sample. The each found α value in Table 4.11 are positive because of the illustration of their typical ISE performance displaying that the plastic deformation is better than the elastic deformation in the superconducting crystal texturing samples. The Sr site Nd substituted level affects the curve properties due to the mechanical durability, stiffness and strength on the structural problems in crystal system. The values of α constants increase from 3.3823×10^{-3} N/μm to 4.2486×10^{-3} N/μm with the increasing of Nd inclusions, confirming that destruction the stabilization in the strong tetragonal phase. Thus, the Nd0 sample displays the best mechanical properties to the applied load. Further, the load independent hardness value (H_{PSR}) is computed as demonstrated in the following relation (75).

$$H_{PSR} = 1854.4\beta \tag{4.23}$$

Based on this result the PSR model are not close to the saturation limit regions.

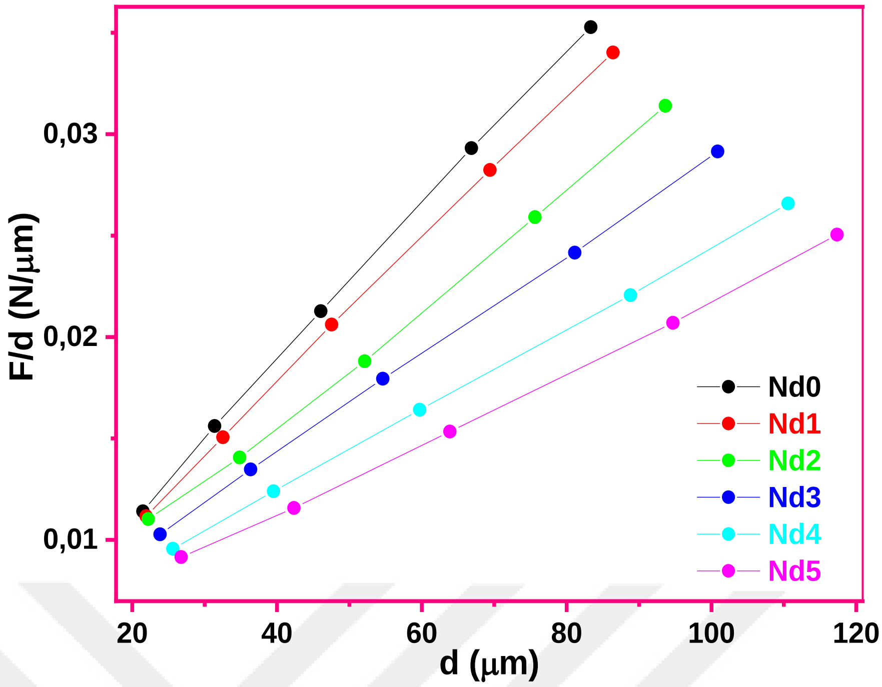

Figure 4.13. Graphs of *F/d* versus *d* for all samples.

Table 4.11. PSR model results for every sample.

Samples	PSR model		H_{PSR}(GPa)	H_V (GPa)
	α x10^{-3} (N/µm)	βx10^{-4}(N/µm^2)		
Nd0	3.3823	3.8523	0.714	0.784 – 0.813
Nd1	3.5444	3.5444	0.657	0.730 – 0.754
Nd2	4.2364	2.8739	0.532	0.621 – 0.635
Nd3	4.5561	2.4329	0.451	0.535 – 0.552
Nd4	4.4859	1.9919	0.369	0.445 – 0.460
Nd5	4.2486	1.7556	0.325	0.395 – 0.405

4.10.3 Elastic / Plastic Deformation Model

The elastic / plastic deformation model allows us to analyse the mechanical properties and load-independent hardness of a material near the saturation boundary regions. The dependency of indentation size on the applied load is computed with formula (76).

$$F = A_{EPD}(d_e + d_p)^2 \qquad (4.24)$$

Figure 4.14 demonstrates the application of equation 4.24 as $F^{1/2}$ versus d_p to the materials results for elastic deformation (d_e) and load independent microhardness constant (A_{EPD}) in Table 4.12. The values of d_e are obtained to be positive for every sample. The existence elastic deformation is attained with plastic deformation for static applied loads describes the ISE performance for every material. Elastic reduction is obtainable for every samples. The de value of pure sample is found 0.07833 µm, while the maximum 0.13205 µm value is attributed to the Nd5 sample. Additionally, the load independent hardness value can be illustrated by equation:

$$H_{EPD} = 1854.4 A_{EPD} \tag{4.25}$$

Besides, Table 4.12 declares that the H_{EPD} hardness parameters are lesser than the true hardness values. Hence, the EPD model is insufficient to examine the original hardness values for the Bi-2223 system.

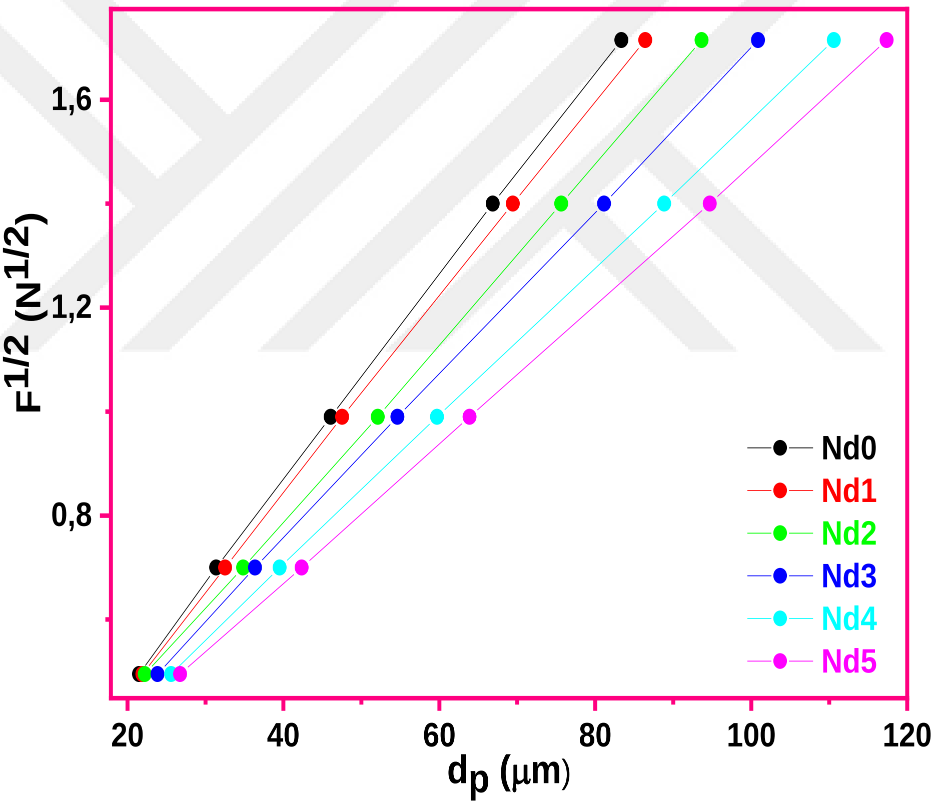

Figure 4.14. Extrapolation curves between $F^{1/2}$ and d_p.

Table 4.12. EPD model results for every sample.

Samples	EPD model		H_{EPD} (GPa)	H_V (GPa)
	d_e (µm)	A_{EPD} (N/µm^2)		
Nd0	0.07833	0.0197	0.719	0.784 – 0.813
Nd1	0.08469	0.0189	0.663	0.730 – 0.754
Nd2	0.10677	0.0171	0.543	0.621 – 0.635
Nd3	0.12338	0.0157	0.461	0.535 – 0.552
Nd4	0.13207	0.0143	0.379	0.445 – 0.460
Nd5	0.13205	0.0134	0.335	0.395 – 0.405

4.10.4 Hays–Kendall Approach

Hays Kendall approach (HK) is more preferred method for studying load-independent microhardness parameters. Kendall and Hays suggested that the association among the indentation size and indentation test load is not the real, but then

$$F_{eff} = F - W_{HK} \tag{4.26}$$

which can be readjusted to

$$F = W_{HK} + A_{HK}d^2 \tag{4.27}$$

where W_{HK} presents minimum test load and A_{HK} is the hardness constant. In the formula, the microhardness parameter of A_{HK} is deduced from the extrapolation of plots among the static applied test load F and indentation diagonal length d^2 as given in Figure 4.14. The hardness constant and minimum test load is represented in Table 4.13. The values of minimum test load are positive for every sample demonstrating ISE properties, so the static applied test load is adequate to generate plastic and elastic deformation. The obtained values of W_{HK} the Nd0 sample is smaller than that of the Nd5 sample. The H_{HK} can be computed by relation:

$$H_{HK} = 1854.4A_{HK} \tag{4.28}$$

We list all the calculations in Table 3. The HK model is sufficiently to the microhardness properties demonstrating the ISE behavior presenting that the HK model is very near to the saturation region (77).

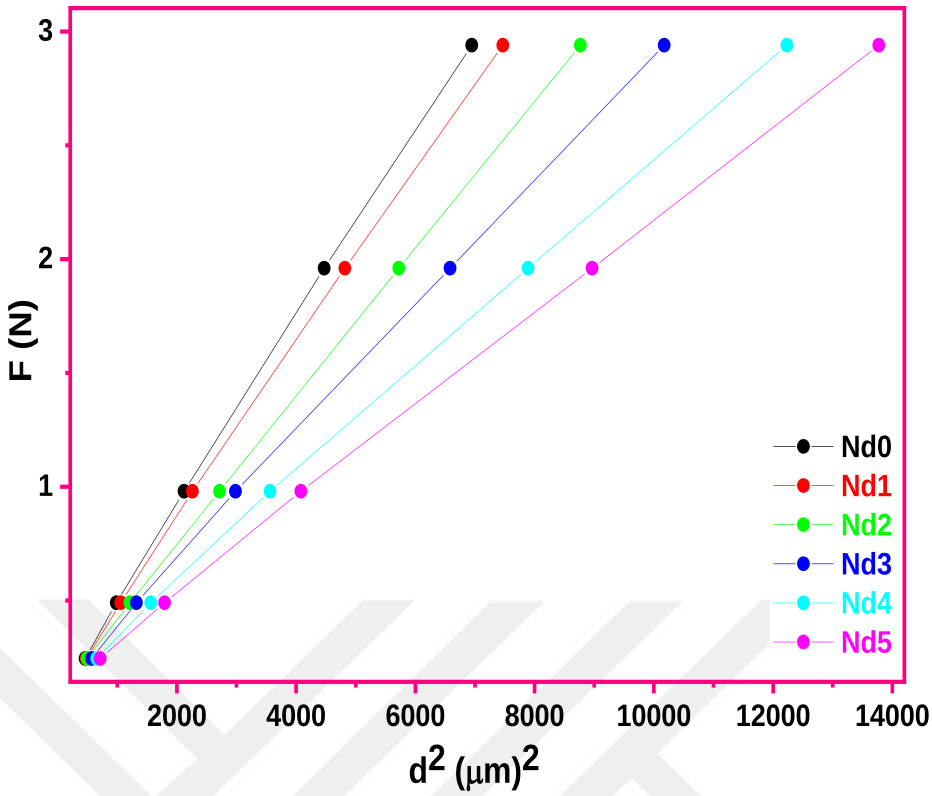

Figure 4.15. Static applied test load against to the square of diagonal length for each material.

Table 4.13. HK approach results for every sample.

Samples	HK model		H_{HK} (GPa)	H_V (GPa)
	A_{HK} x10^{-4} (N/μm^2)	W_{HK} (N)		
Nd0	4.1486	0.07833	0.769	0.784 – 0.813
Nd1	3.8494	0.08469	0.713	0.730 – 0.754
Nd2	3.2537	0.10677	0.603	0.621 – 0.635
Nd3	2.7876	0.12338	0.516	0.535 – 0.552
Nd4	2.3138	0.13207	0.429	0.445 – 0.460
Nd5	2.0533	0.13205	0.380	0.395 – 0.405

4.10.5 Evaluation of Real Vickers Microhardness Values Attributed to Modified Proportional Sample Resistance Model

Modified proportional sample resistance is a model to examine the mechanical features and true micro hardness parameters of a material in the plateau regions. This model is a method for determining the ISE or RISE properties of the materials and can be defined with the formula:

$$F = W_{MPSR} + A_{MPSR}d + B_{MPSR}d^2 \qquad (4.29)$$

In the formula, W_{MPSR} is minimum static applied test load for indentation and the constant of A_{MPSR} and B_{MPSR} is attributed to the energy loss values established on the permanent deformation of a unit volume and statistically gathered in Table 4.14. Hence, the formula is described as the distinction of applied load according to the diagonal length shown in Figure 4.16. As seen from the table, A_{MPSR} parameters are positive for pure and Sr site Nd substituted Bi-2223 system due to the nature of the ISE. In this context, elastic and plastic deformations are generated in all samples. We examine the true hardness values using the MPSR model:

$$H_{MPRS} = 1854.4A_{MPSR} \qquad (4.30)$$

All calculations in Table 4.14 can be seen. The H_{MPSR} values reduce with the increment of the Sr-site Nd substituted level while being smaller than the values of the saturation boundary region. Therefore, the MPSR model is not sufficient to determine the true micro hardness value (78).

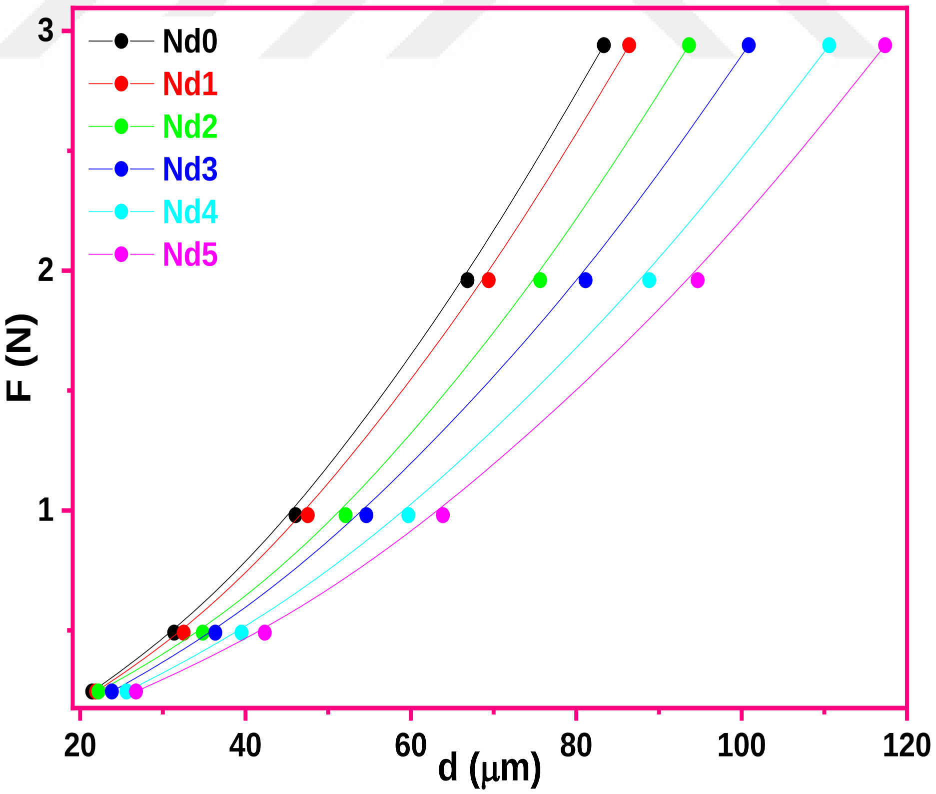

Figure 4.16. Change of the *F* versus the *d* for all the samples.

Table 4.14. MPSR model results for every sample.

Samples	MPSR model			H_{MPSR} (GPa)	H_V (GPa)
	W_{MPSR} (N)	A_{MPSR} x10^{-3} (N/µm)	B_{MPSR}x10^{-4} (N/µm^2)		
Nd0	-0.04744	5.7917	3.6101	0.669	0.784 – 0.813
Nd1	-0.03685	5.3619	3.3676	0.624	0.730 – 0.754
Nd2	0.06266	1.2336	3.1503	0.584	0.621 – 0.635
Nd3	0.00554	4.348	2.4486	0.454	0.535 – 0.552
Nd4	0.01250	4.0016	2.0283	0.376	0.445 – 0.460
Nd5	0.04976	2.3301	1.8964	0.351	0.395 – 0.405

4.11 Microhardness Properties Investigated by Dynamic Micro-Indentation Method

4.11.1 Theoretical Background of Dynamic Microhardness

To make measurements in traditional indentation methods, the test load is exerted to the surface of the superconducting material and then the indentation is extracted from the sample. There is no role in elastic deformation in predictable hardness tests. Hardness (*H*) and elastic modulus (E_r) are computed with both depth and load through elastic and plastic deformation from an unloading curve, and it is not necessary to attain the diagonal of the indented print with a system of optical (79). Figure 4.16 demonstrate that a view of the indentation and load-depth curve extracted from measurement of the dynamic indentation. Throughout the loading-unloading advance the material is subjected to plastic and elastic deformation. The h_{max} (h_f) values present the maximum (final) contact depth in the Figure 4.16. The indentation hardness is described by the following formula:

$$H = \frac{P_{max}}{A_c} = \frac{P_{max}}{24.5h_c^2} \qquad (4.31)$$

where h_c is the contact depth, $Ac = \pi h_c^2 tan^2\alpha = 24.5h_c^2$ is the area of the indentation printing and P_{max} illustrate the peak load deduced form the unloading curve as depicted in Figure 4.17. The contact area is $A_c = 24.5h_c^2$ and consequently the half-angle of an equivalent conical indentation is 70.3^0 for the Berkovich indenter. Different approaches are found to obtain the values of h_c from the unloading curves. This approach begins with appropriate the unloading curve to power-law relationship:

$$P = a(h - h_f)^m \tag{4.32}$$

here h displays the diagonal length, P present the load, h_f demonstrates the final depth and m is the fitting parameters. By using first part of the unloading curve the value of stiffness (S) is computed following equation:

$$S = \left|\frac{dP}{dh}\right| = \frac{2}{\sqrt{\pi}} E_r \sqrt{A_c} \tag{4.33}$$

in here, E_r demonstrate the reduced elastic modules (80). Experimental data of visible microhardness are used to attain the real hardness values.

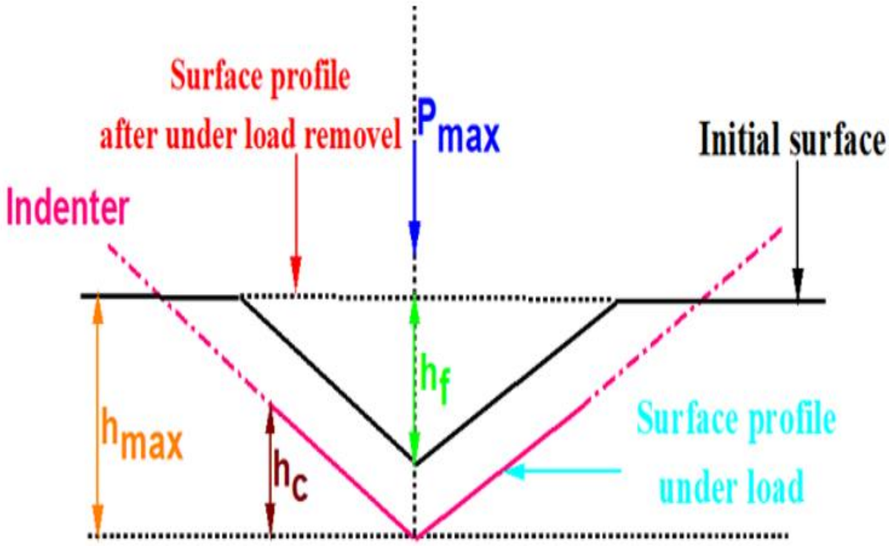

Figure 4.17. Cross-section view of indentation

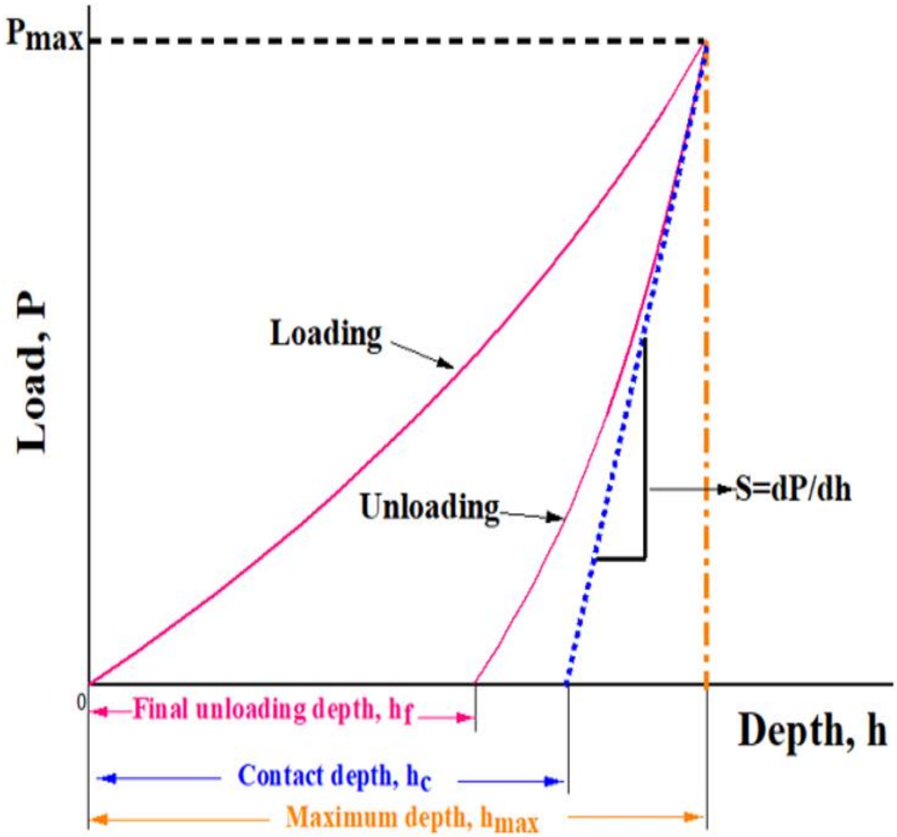

Figure 4.18. Schematic illustration of a characteristic load–depth curve displaying the values used in the Oliver and Pharr Method

4.11.2 Investigating of Load-Displacement Curves

The dependency of unload/load on contact depth for pure and Nd/Sr partial replacement in Bi-2223 superconducting ceramic samples for different load magnitudes are shown in Figure 4.19. The values of load (P_{max}), contact depth (h_c), stiffness (S), hardness (H) and elastic modulus (E_r) are summarized in Table 4.15. There is small scattering in the load / unload depth curves for all samples. These scattering may be caused by structural inhomogeneity. The h_c values increment with the applied load up to the Nd4 sample, beyond which the values changed randomly and this is confirming increase of porosity in SEM (Table 4.15.).

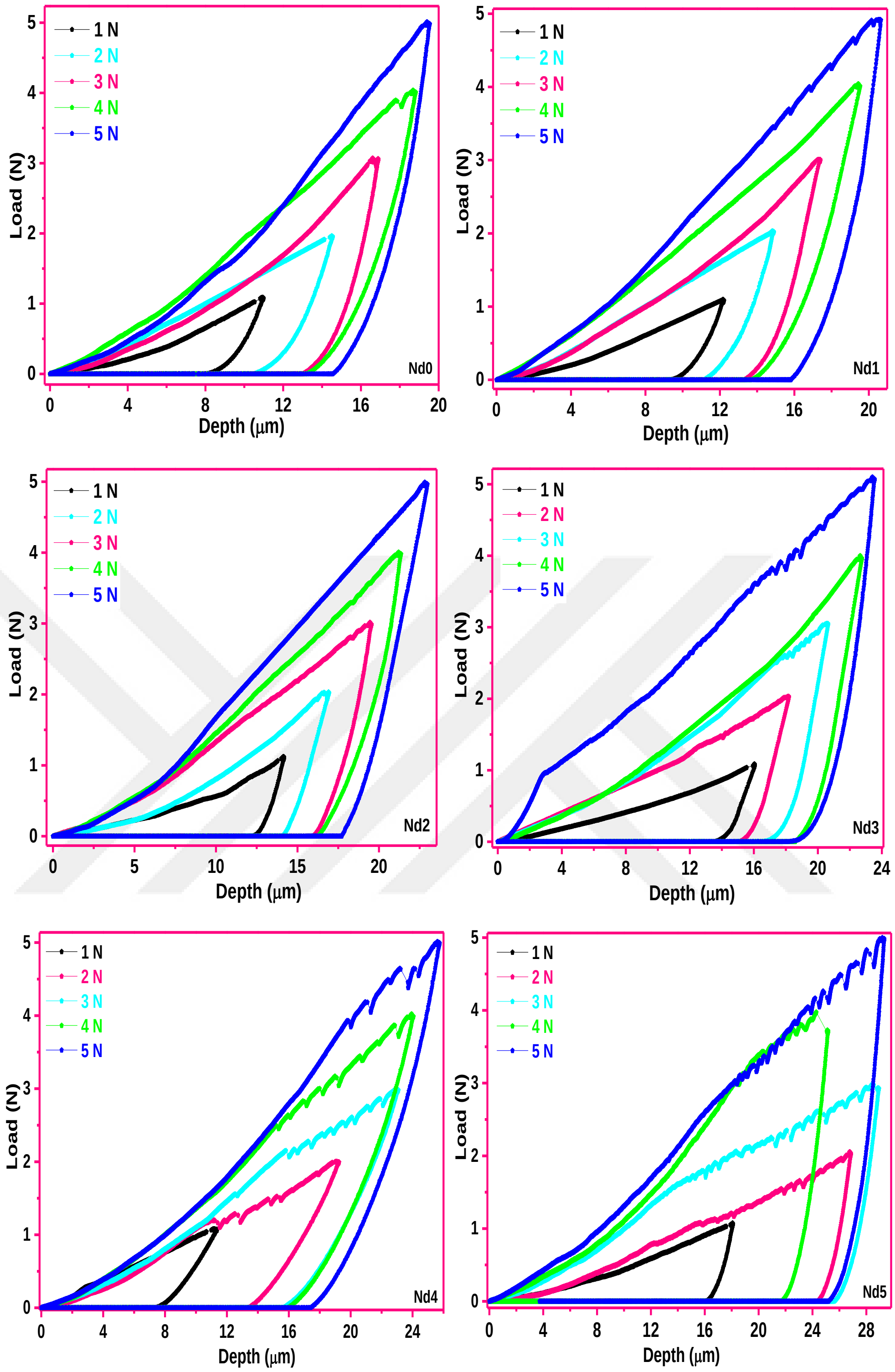

Figure 4.19. Loading/unloading-depth curve for every samples.

4.11.3 Microhardness Characteristics Study by Dynamic Micro-Indentation Technique

The experimental result of the *H* values as a function of applied load are demonstrated in Figure 4.20. The dynamic microhardness values (*H*) increment with the applied load up to Nd4 samples (except Nd4 sample at 1.0 N applied load), after which this parameter changes randomly for the Nd5 sample (Table 4.15). This is attributed the fact that the SEM investigation has more voids and porosity in Nd5 sample.

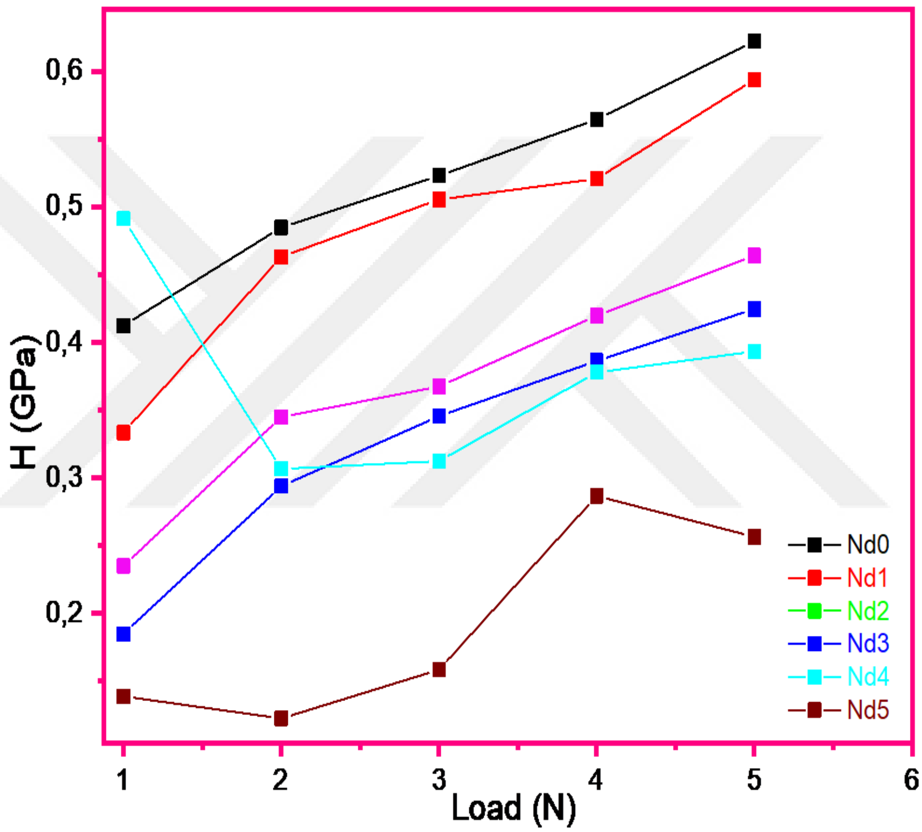

Figure 4.20. Dynamic hardness values as function of applied load.

4.11.4 Reduced Elastic Modulus

The experimental obtained reduced elastic modulus versus applied load as illustrated in Figure 4. 21 and the value of E_r gathered in Table 4.15. As can be seen from the table that the E_r values increase with enhancement peak load except for Nd5 at 2.0 N applied load. The minimum reduced elastic modulus (E_r) obtained for the Nd4 sample, due to difference of h_{max}-h_c values are greatest that of all the samples.

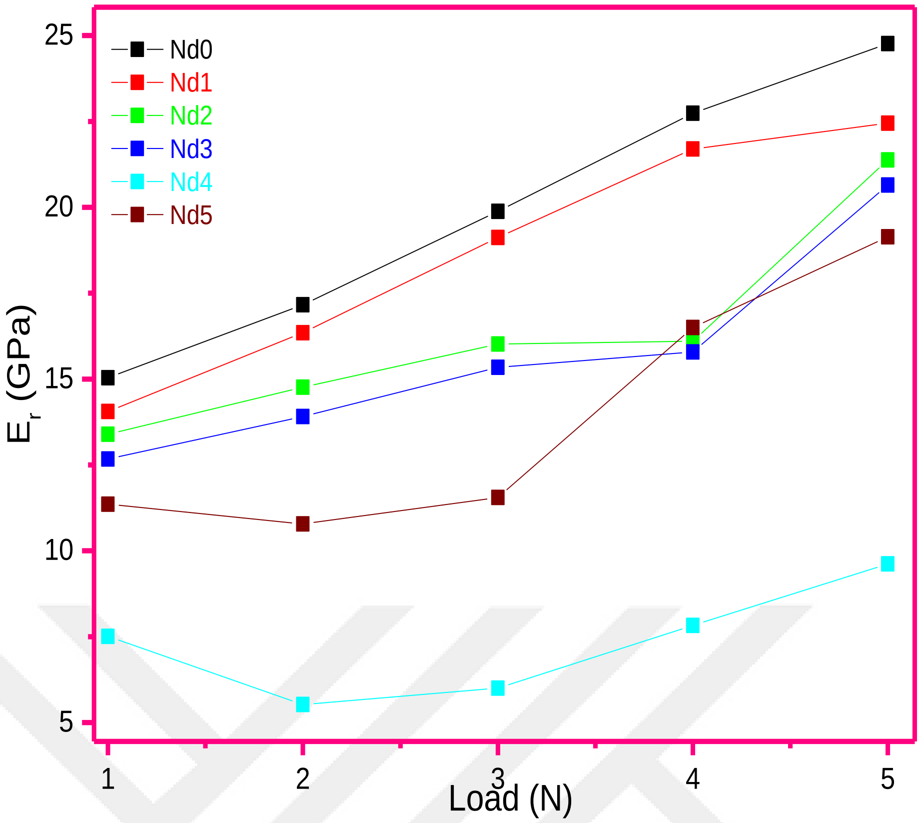

Figure 4.21. Reduced elastic modulus values as function of applied load.

4.11.5 Calculation of Stiffness Parameters

The stiffness (*S*) can be described as the resistance of a sample to variation in length in corresponds to the load. The *S* values are estimated by using the unloading curve with the aid of equation 4.33 and are showed in Table 4.15. The values of *S* increase with increasing applied load for all the samples (Table 4.15).

Table 4.15. P_{max}, h_c, S, H and E_r values for samples.

Samples	P_{max} (N)	h_c (µm)	H (GPa)	E_r (GPa)	S (N/ µm)
Nd0	1.0	10.0717	0.4126	15.038	0.845
	2.0	12.9612	0.4849	17.163	1.242
	3.0	15.2996	0.5231	19.883	1.699
	4.0	16.9892	0.5646	22.737	2.157
	5.0	18.0135	0.6222	24.768	2.491
Nd1	1.0	11.0625	0.3335	14.055	0.868
	2.0	13.2734	0.4633	16.347	1.211
	3.0	15.5629	0.5055	19.122	1.662
	4.0	17.7044	0.5207	21.696	2.145
	5.0	18.5345	0.5940	22.447	2.323
Nd2	1.0	13.1700	0.2352	13.391	0.985
	2.0	15.3801	0.3450	14.762	1.268
	3.0	18.1455	0.3676	16.020	1.623
	4.0	19.6386	0.4197	16.101	1.766
	5.0	20.9698	0.4641	21.380	2.504
Nd3	1.0	15.1334	0.1851	12.673	1.071
	2.0	16.6578	0.2940	13.908	1.293
	3.0	18.7921	0.3457	15.344	1.610
	4.0	20.5549	0.3864	15.790	1.812
	5.0	22.0071	0.4247	20.646	2.537
Nd4	1.0	9.29730	0.4914	7.507	0.389
	2.0	16.2622	0.3067	5.527	0.502
	3.0	19.6785	0.3125	6.002	0.659
	4.0	20.7251	0.3780	7.825	0.905
	5.0	22.6572	0.3934	9.619	1.217
Nd5	1.0	17.3810	0.1390	11.358	1.102
	2.0	25.8356	0.1227	10.782	1.555
	3.0	27.6664	0.1586	11.551	1.784
	4.0	23.7735	0.2868	16.500	2.190
	5.0	28.0652	0.2567	19.141	3.000

4.11.6 Pop In and Pop Out Properties

Another significant parameter of mechanical performance is pop in and pop out feature. The pop out performance can be found in the unloading part whereas the pop in nature is deduced from the loading part of the measurement as seen from the Figure 4.19. The multiple pop in event of the sample studied are not observed for 1 N applied load, after which the pop in begins to appear because of the existence of dislocations, voids and cracks. Moreover, there are no apparent pop-out case of indentation loop of samples. Based on these result that every samples can play a significant effect in preventing the formation of mechanical breaks by affecting the structure.

4.11.7 Indentation-Induced Cracking Model

The experimental data are used to obtain the true hardness values for Sr/Nd replacement in Bi-2223 superconducting ceramics by means of the Indentation-induced cracking (IIC) model. Besides, the hardness values (H_{IIC}) are extracted from experimental data following equation (81, 82):

$$H_{IIC} = K(\frac{P^{5/3}}{h_c^3})^m \tag{4.34}$$

The K and m values are estimated from the slopes of the $L_n(H) - L_n(P^{5/3}/h_c^3)$ curve and the real microhardness (H_{IIC}) values are determined from the vertical intercept of the graph. Further, the extracted values of K and m are gathered in Table 4.16. The m parameters can be used to define the type of ISE nature for $m > 0.6$, while $m < 0.6$ points out the RISE feature. According to the table that the m parameters are obtained greater than 0.6 for the Nd4 samples, confirming that the sample show the ISE behavior. Moreover, the Nd0, Nd1, Nd2, Nd3 and Nd5 samples demonstrate the RISE behavior due to the m parameters lower than 0.6 (83).

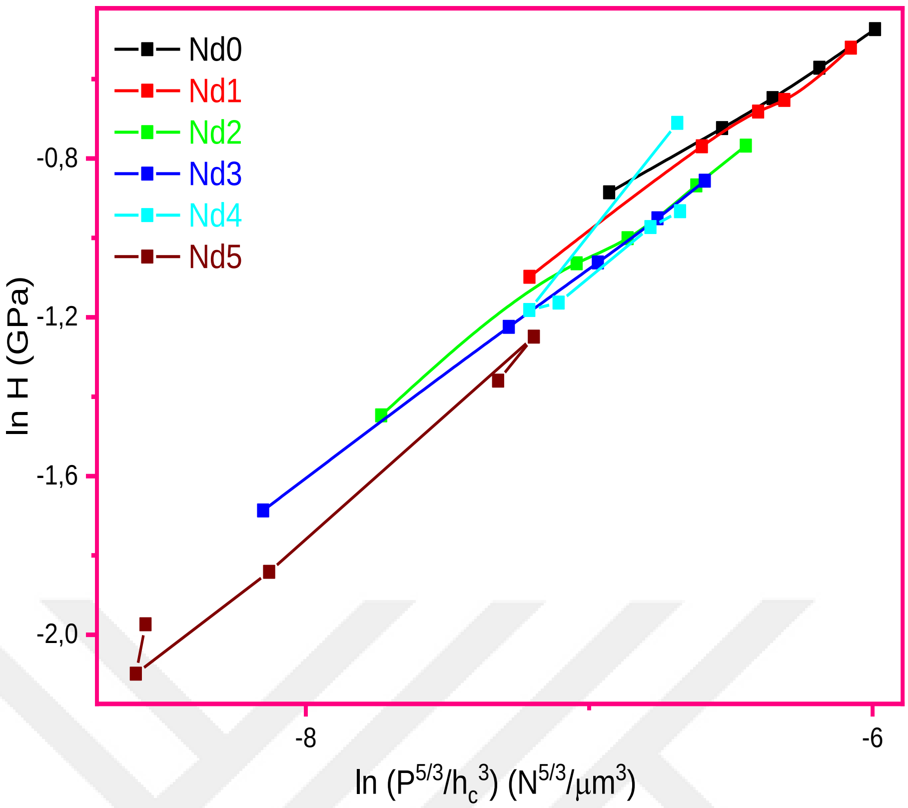

Figure 4.22. ln(H)-ln($P^{5/3}/h_c^3$) curves of the samples.

Table 4.16. *K*, *m* and H_{IIC} values for samples.

Samples	Kx10^4 ($N^{(3-5mA)/3}/\mu m^{(2-3m)}$)	m	H_{IIC} (GPa)
Nd0	0.000837	0.435	0.522
Nd1	0.001271	0.504	0.483
Nd2	0.002803	0.522	0.764
Nd3	0.001400	0.530	0.327
Nd4	0.004207	0.686	0.375
Nd5	0.001567	0.559	0.193

5. CONCLUSIONS

In the present work, the influences of aliovalent Nd/Sr partial substitution in the $Bi_{1.8}Pb_{0.35}Sr_{1.9-y}Nd_yCa_{2.2}Cu_3O_x$ crystal lattice within the molar ratio between 0.00 and 0.10 on the electrical, superconducting, crystallinity, surface morphology view and crystallinity quality features are inspected with the aid of temperature-dependent electrical resistivity, powder X-ray diffraction, scanning electron microscopy, flux pinning mechanism, Vickers microhardness, electron dispersive X-ray and magnetization-magnetic field measurements (MH). The conclusions can be explained by the following findings:

- The Nd0 sample possesses the maximum onset and offset critical transition temperatures of 116.59 K and 108.40 K while the Nd5 sample exhibits the global minimum characteristic temperatures of 108.74 K for the onset and 78.81 K for the offset transition temperature.
- The ρ_{300K} value of un-replaced compound is recorded as about 0.0140 Ωcm whereas the Nd1 sample exhibits the value of about 0.0146 Ωcm followed by a relatively rapid increment for other materials. In case of the maximum substitution level, the ρ_{300K} value climbs to the top point of 0.0232 Ωcm.
- The un-substituted Bi-2223 compound exhibits such a ΔT_c value of 8.19 K whereas the Nd5 sample shows the maximum value of 29.93 K.
- The P_{hole} is found to decrease dramatically from 0.14673 until the global minimum value of 0.10141 with increasing the Nd/Sr substitution level.
- The characteristic high-T_c Bi-2223 superconducting volume fraction is noted to reduce with the increment in the Nd purity. On the other hand, the low-T_c Bi-2221 superconducting phase tends to enhance importantly with the substitution.
- A regular reduction in the *c*-axis length is obtained while a systematic increasing in the *a*-axis length is found with increment the Nd/Sr substitution level.
- The Nd0 sample founds the narrowest FWHM value, displaying the highest average crystallite size (59.3 nm) and best crystallinity and connectivity between grains.

- The experimental XRD curves indicate that the existence of Nd nanoparticles causes to disappear some peaks of (002) H, (004) H, (008) H, (0020) H, (315) H, (317) H and (319) H in the XRD diffractograms.
- The Nd0 sample has well linked flaky layers, and thus shows the most uniform surface structure among the materials.
- EDX analysis shows that the chemical contents of Bi, Pb, Sr, Ca, Cu and O tend to change randomly, while the atomic distribution of Nd has been found to increase systematically as expected.
- The best J_c value is found from magnetization measurement for the un-replaced sample.
- The flux pinning energy values tend to decrease methodically, with the increment of both Nd replacement and magnetic field.
- The μH_{irr} and μH_{c2} values decrement with increase of Nd impurities because of the reduce in the pinning capability attributed to the pinning force.
- Every ξ (0) and λ (0) value tends to increase methodically depending on the Nd replacement in the Bi-2223 system.
- The Vickers hardness for all samples reduces non-linearly with the enhance in the applied load up to 2 N, beyond which a small change is found owing to the influence of the plateu region, comfirming that the surface effect becomes more dominant.
- The maximum H_v value is found as 0.984 GPa for pure sample.
- The properties of ISE behavior are found to deteriorate methodically with the Nd addition.
- Hays Kendall approach gives results much closer to the load-independent Vickers microhardness parameters near the saturation boundary regions compared to the other models.
- The load independent microhardness values for Meyer's law, PSR, EPD and MPSR models are lower than the load dependent hardness values in saturation region, and hence these models are insufficient for the determination of the original microhardness value of the Nd replacement in Bi-2223.

- The dynamic hardness values enhance with the applied load (except for the Nd4 sample at 1.0 N), while these values are obtained to vary randomly for the Nd5 sample.
- The minimum Er values are found for Nd4 sample, comfirming that the (h_{max} - h_c) values are highest than the other samples.
- The stiffness values increment with the increase of the applied load for all samples.
- The pop-in is attained for all the samples except at 1.0 applied load, while the pop-out is not found for all samples.

6. REFERENCES

"Vancouver citation system was used in this thesis."

1. Onnes HK. The resistance of pure mercury at Helium temperatures. Commun. Phys. Lab. Univ. Leiden. 1911;12:120.

2. London F, London H. The electromagnetic equations of the supraconductor. Proc. Roy. Soc. 1935;149:71.

3. Abrikosov AA. On the magnetic properties of superconductors of the second group. Soviet Physics JETP. 1957;5:1174.

4. Bednorz JG, Muller KA. Possible high T_c superconductivity in the Ba-La-Cu-O system. Z. Phys. B. Condensed Matter. 1986;64(1):189–193.

5. Wu MK, Ashburn JR, Torng CJ. Superconductivity at 93-k in a new mixed-phase y-ba-cu-o compound system at ambient pressure. Phys. Rev. Lett. 1987;58(9):908–910.

6. Michel C, Hervieu M, Borel MM, Grandin A, Deslandes F, Provost J, Raveau B. Superconductivity in the Bi- Sr- Cu- O System. Z. Phys. B. Cond. Matter. 1987;68:421–423.

7. Maeda H, Tanaka Y, Fukutomi M, Asano T. A new high-T_c oxide superconductor without a rare earth element. Jpn. J. Appt. Phys. 1988;27(2):209–210.

8. Togano K, Kumakura H, Maeda H, Yanagisawa E, Takahashi K. Properties of Pb doped BiSrCaCuO superconductors. Appl. Phys. Lett. 1988;53:1329.

9. Hazen MR, Finger LW, Angel RJ, Prewith TC, Ross RL, Hermann AM. 100-K Superconducting Phases in the Tl-Ca-Ba-Cu-O System. Phys. Rev. Lett. 1998;60:1657–1662.

10. Sheng ZZ, Hermann AM. Bulk superconductivity at 120 K in the Tl–Ca/Ba–Cu–O system. Nature. 1988;332:138–139.

11. Iqbal Z, Datta T, Kirven D, Longu A, Barry JC, Owens FJ, Rinzler AG, Yang D, Reidinger F. Superconductivity above 130 K in the Hg-Pb-Ba-Ca-Cu-O system. Phys. Rev. B 1994;49:12322–12326.

12. Schilling A, Cantoni M, Guo JD, Ott HR. Superconductivity above 130 K in the Hg-Ba-Ca-Cu-O system. Nature. 1993;363:56–57.

13. Nagamatsu J, Nakagawa N, Muranaka T, Zenitani Y, Akimitsu J. Superconductivity at 39 Kin magnesium diboride. Nature. 2001;410:63–64.

14. Meissner W, Ochsenfeld R. Ein neuer effekt bei eintritt der supraleitfahigkeit. Naturwissenschaften. 1933;21(44):787–788.

15. Cyrot M, Pavuna D. Introduction to superconductivity and High-Tc Materials. Singapore. 1992.

16. Charles K. Introduction to solid state physics. Seventh edition, Wiley India; 2004.

17. Bardeen J, Cooper LN, Schrieffer JR. Theory of superconductivity. Phys. Rev. 1957;108(5):1175.

18. Ginsburg VL, Landau LD. On the Theory of superconductivity. Zh. Eksp. Teor. Fiz. 1950;20:1064–1082.

19. Owens FJ, Poole JCP. Selected Topics in Superconductivity the New Superconductors. New York; 2002.

20. Sheahen TP. Introduction to High-Temperature Superconductivity. 1st edn. Springer; 1994.

21. Mousavi GSE, Zargar SM. Structural and physical properties of Cd-doped $Bi_{1.64}Pb_{0.36}Sr_2Ca_{2-x}Cd_xCu_3O_y$ superconductor. Physica B. 2010;405:4643–4649.

22. Omar MA. Elementary Solid-State Physics. Addison-Wesley; 1993.

23. Takayama ME. High-pressure synthesis of homologous series of high critical temperature (T_c) superconductors. Chem. Mater. 1998;10:2686–2698.

24. Yamauchi H, Karppinen M. Application of high-pressure techniques: stabilization and oxidation-state control of novel superconductive and related multi-layered copper oxides. Supercond. Sci. Techol. 2000;13:R33–R52.

25. Karpinski J, Meijer GI, Schwer H, Molinski R, Kopnin E, Conder K, Angst M, Jun J, Kazakov S, Wisniewski A, Puzniak P, Hofer J, Alyoshin V, Sin A. High pressure synthesis, crystal growth, phase diagrams, structural and magnetic properties of $Y_2Ba_4Cu_nO_{2n+x}$, $HgBa_2Ca_{n-1}Cu_nO_{2n+2+\&}$ and quasi one-dimensional cuprates. Supercond. Sci. Technol. 1999;12:R153–R181.

26. Lehndorff BR. High-T_c Superconductors for Magnet and Energy Technology. 1st. Ed. Springer; 2001.

27. Yildirim G, Bal S, Yucel E, Dogruer M, Akdogan M, Varilci A, Terzioglu C. Effect of Mn Addition on Structural and Superconducting Properties of (Bi, Pb)-2223 Superconducting Ceramics. J. Supercond. Nov. Magn. 2012;25:381–390.

28. Bal S, Dogruer M, Yildirim G, Varilci A, Terzioglu C, Zalaoglu Y. Role of Cerium Addition on Structural and Superconducting Properties of Bi-2212 System. J. Supercond. Nov. Magn. 2012;25:847–856.

29. Ozturk O, Asikuzun E, Kaya S, Coskunyurek M, Yildirim G, Yilmazlar M, Terzioglu C. Physical Properties and Diffusion-Coefficient Calculation of Iron Diffused Bi-2223 System. J. Supercond. Nov. Magn. 2012;25:2481–2487.

30. Guner SB, Gorur O, Celik S, Dogruer M, Yildirim G, Varilci A, Terzioglu C. Effect of zirconium diffusion on the microstructural and superconducting properties of $YBa_2Cu_3O_{7-x}$ superconductors. J. Alloy. Compd. 2012;540:260–266.

31. Gohring D, Vogt M, Wischert W, Kemmler-Sack S. Doping of (Bi, Pb)-2223 with metal oxides. Mater. Sci. Eng. B: 1997;48:244–253.

32. Dou SX, Liu HK, Guo SJ, Easterling KE, Mikael J. Superconductivity in the Bi-Pb-Sr-Ca-Cu-O system with oxide additions. Supercond. Sci. Technol. 1989;2:274–278.

33. Sasakura H, Akagi Y, Tsukui S, Adachi M. Effect of Boron Substitution for Bi on Superconductivity of the Bi-2212 Phase in the Bi-Sr-Ca-Cu-O System. J. Supercond. Nov. Magn. 2010;23:437–441.

34. Ianculescu A, Gartner M, Despax B, Bley V, Lebey Th, Gavrila R, Modreanu M. Optical characterization and microstructure of $BaTiO_3$ thin films obtained by RF-magnetron sputtering. Appl. Surf. Sci. 2006;253:344–348.

35. Mangapathi Rao D, Somaiah T, Haribabu V, Venudhar YC. Growth kinetics of high- T_c, and low- T_c, phases in $Bi_{2-x}Pb_xCa_2Sr_2Cu_3O_y$, superconducting compounds. Cryst. Res. Technol. 1993;28:285–298.

36. Kocabas K, Ozkan O, Bilgili O, Kadıoglu Y, Yılmaz H. The Effects of Mg Substitution in Bi-2223 Superconductors. J. Supercond. Nov. Magn. 2010;23:1485–1492.

37. Azzouz BF, Mchirgui A, Yangui B, Boulesteix C, Salem BM. Synthesis, microstructural evolution and the role of substantial addition of PbO during the final processing of (Bi, Pb)-2223 superconductors. Phys. C. 2001;356:83–96.

38. Yildirim G, Yucel E, Bal S, Dogruer M, Varilci A, Akdogan M, Terzioglu C, Zalaoglu Y. Investigation of Structural and Superconducting Properties of Cr Added Bi-2212 Superconducting Ceramics. J. Supercond. Nov. Magn. 2012;25:231–237.

39. Aydın H, Babanli A, Altintas SP, Asikuzun E, Soylu N, Ozturk O, Dogruer M, Terzioglu C, Yildirim G. Breaking point of the harmony between Gd diffused Bi-2223 slabs with diffusion annealing temperature. J. Mater. Sci. Mater. El. 2013;24:4566–4573.

40. Gorur O, Yildirim G, Altintas SP, Terzioglu C. Role of Gd content in Cu(1) and Cu(2) sites on electrical, microstructural, physical, mechanical and superconducting properties of $YBa_2Cu_{3-x}Gd_xO_{7-\delta}$ ceramics. J. Mater. Sci. Mater. El. 2013;24:1842–1854.

41. Dogruer M, Yildirim G, Yucel E, Terzioglu C. Role of diffusion-annealing temperature on the microstructural and superconducting properties of Cu doped MgB_2 superconductors. J. Mater. Sci. Mater. El. 2012;23:1965–1970.

42. Ozturk O, Asikuzun E, Erdem M, Yildirim G, Yildiz O, Terzioglu C. The effect of Pr addition on superconducting and mechanical properties of Bi-2212 superconductors. J. Mater. Sci. Mater. El. 2012;23:511–519.

43. Aksan MA, Yakinci ME, Kadowaki K. The Effect of Ru Substitution on the Thermal, Structural and Magnetic Properties of $Bi_3Sr_2Ca_2Cu_3O_\delta$ Superconducting System. J. Supercond. Nov. Magn. 2010;23:371–380.

44. Bilgili O, Selamet Y, Kocabas K. Effects of Li Substitution in Bi-2223 Superconductors. J. Supercond. Nov. Magn. 2008;21:439–449.

45. Malachevsky MT, Dovidio CA. SEM investigation of the critical current degradation onset in BSCCO-2223 multifilamentary tapes submitted to bending. Supercond. Sci. Technol. 2005;18:289–293.

46. Akdogan M, Terzioglu C, Varilci A, Belenli I. Diffusion coefficient, activation energy and the effect of Ag-doping on some physical properties of silver doped $Bi_{1.8}Pb_{0.4}Ca_{2.2}Sr_2Cu_3O_x$. Phys. B. 2010;405:4010–4019.

47. Ozturk O, Erdem M, Asikuzun E, Yildiz O, Yildirim G, Varilci A, Terzioglu C. Investigation of indentation size effect (ISE) and micro-mechanical properties of Lu added $Bi_2Sr_2CaCu_2O_y$ ceramic superconductors. J. Mater. Sci. Mater. El. 2013;24:230–238.

48. Yildirim G. Beginning point of metal to insulator transition for Bi-2223 superconducting matrix doped with Eu nanoparticles. J. Alloy. Compd. 2013;578:526–535.

49. Dogruer M, Terzioglu C, Yildirim G. Effect of MgB_2 addition on thermal fluxon motions of two dimensional pancake vortices in Bi-2223 superconducting ceramics. J. Alloy. Compd. 2017;727:879–886.

50. Ozcelik B, Kaya C, Gundogmus H, Sotelo A, Madre MA. Effect of Ce Substitution on the Magnetoresistivity and Flux Pinning Energy of the $Bi_2Sr_2Ca_{1-x}Ce_xCu_2O_{8+\delta}$ Superconductors. J. Low Temp. Phys. 2014;174:136–147.

51. Mua NT, Sundaresan A, Man NK, Dung DD. Influence of preparation conditions on superconducting properties of Bi-2223 thin films. Bull. Mater. Sci. 2014;37:19–25.

52. Mourachkine A. Room-temperature Superconductivity. second ed., Cambridge international science publishing, Cambridge; 2004.

53. Abrikosov AA, Gorkov LP. Theory of superconducting alloys with paramagnetic impurities. Zh. Eksp. Teor. Fiz. 1960;39:1781–1796.

54. Kusevic I, Simundic P, Babic E, Ivkov J, Marohnic Z, Ionescu M, Lui HK, Dou SX. J(c)-B-T Surface of High-J(c) $Bi_2Sr_2CaCu_2O_{8+x}$/Ag tape. Supercon. Sci. Technol. 1996;9:1060–1065.

55. Zalaoglu Y, Yildirim G, Buyukuslu H, Saritekin NK, Varilci A, Terzioglu C, Gorur O. Important Defeats on pinning of 2D pancake vortices in highly anisotropic Bi-2212 superconducting matrix with Homovalent Bi/La substitution. J. Alloy. and Compd. 2015;631:111–119.

56. Dogruer M, Yildirim G, Terzioglu C. Effect of diffusion-annealing time on magnetoresistivity of Cu-diffused bulk MgB_2 superconductors with experimental and theoretical approaches. J. Mater. Sci. Mater. El. 2013;24:958–967.

57. Zalaoglu Y, Yildirim G, Terzioglu C. Magnetoresistivity study on Cr Added Bi-2212 superconductor ceramics with experimental and theoretical approaches. J. Mater. Sci. Mater. El. 2013;24:239–247.

58. Ambegaokar V, Halperin BI. Voltage due to thermal noise in the dc Josephson effect. Phys. Rev. Lett. 1969;22:1364–1366.

59. Gaffney C, Petersen H, Bednar R. Phase-slip analysis of the nonohmic transition in granular $YBa_2Cu_3O_{6.9}$. Phys. Rev. B. 1993;48:3388–3392.

60. Khosroabadi H, Daadmehr V, Akhavan M. Magnetic transport properties and hall effect in $Gd_{1-x}Pr_xBa_2Cu_3O_{7-y}$ system. Phys. C. 2003;384:169–177.

61. Mohammadizadeh MR, Akhavan M. Magnetoresistance in $Gd(Ba_{2-x}Pr_x)Cu_3O_{7+\delta}$ system. Phys. C. 2003;390:134–142.

62. Kim JH, Dou SX, Shi DQ, Rindfleisch M, Tomsic M. Study of MgO formation and structural defects in in-situ processed MgB_2/Fe wires. Supercond. Sci. Technol. 2007;20:1026–1031.

63. Kitaguchi H, Matsumoto A, Hatakeyama H, Kumakura H. High temperature performance of MgB_2 powder-in-tube composite Tapes. Supercond. Sci. Technol. 2004;17:S486–S489.

64. Yadav CS, Paulose PL. Upper critical field, lower critical field and critical current density of $FeTe_{0.60}Se_{0.40}$ single crystals. New J. Phys. 2009;11:103046.

65. Yildirim G, Dogruer M, Ozturk O, Varilci A, Terzioglu C, Zalaoglu Y. Effect of Ce Addition on the Magnetoresistivity, Irreversibility Field, Upper Critical Field and Activation Energies of Bi-2212 Superconducting Ceramics. J. Supercond. Nov. Magn. 2012;25:893–903.

66. Boudjadja Y, Amira A, Saoudel A, Amirouche L, Mahamdioua N, Varilci A, Altintas SP, Terzioglu C. Effect of Yttrium Doping on Magneto-transport Properties of Bi(Pb)-2212 Superconductors. J. Supercond. Nov. Magn. 2013;26:913–917.

67. Mishra DR, Sharma SV, Sharma RG. Role of vanadium in Bi-2223 ceramics. J. Phys. 2000;54:317–330.

68. Ozturk H, Safran S. Effects of carbon-encapsulated nano boron addition on superconducting parameters of BSCCO. J. Alloy. Compd. 2018;731:831–838.

69. Dogruer M, Gorur O, Karaboga F, Yildirim G, Terzioglu C. Zr diffusion coefficient and activation energy calculations based on EDXRF measurement and evaluation of mechanical characteristics of $YBa_2Cu_3O_{7-x}$ bulk superconducting ceramics diffused with Zr nanoparticles. Powder Technol. 2013;246:553–560.

70. Dogruer M, Terzioglu C, Yildirim G, Pakdil M, Zalaoglu Y. Decrement of crack propagation in bulk Bi-2223 superconducting ceramics with Sn-diffusion annealing temperature. J. Mater. Sci. Mater. El. 2015;26:6013–6019.

71. Zalaoglu Y, Karaboga F, Terzioglu C, Yildirim G. Improvement of mechanical performances and characteristics of bulk Bi-2212 materials exposed to Au diffusion and stabilization of durable tetragonal phase by Au. Ceram. Int. 2017;43:6836–6844.

72. Dogruer M, Terzioglu C, Yildirim G, Gorur O. Significant Change in Mechanical Properties of $YBa_2Cu_3O_{7-x}$ Bulk Superconductors Diffused with Sn Nanoparticles. J. Supercond. Nov. Magn. 2014;27:755–761.

73. Asikuzun E, Ozturk O, Cetinkara HA, Yildirim G, Varilci A, Yılmazlar M, Terzioglu C. Vickers hardness measurements and some physical properties of Pr_2O_3 doped Bi-2212 superconductors. J. Mater. Sci. Mater. El. 2012;23: 1001–1010.

74. Celik S, Ozturk O, Coskun E, Sarıhan M, Asikuzun E, Ozturk K, Terzioglu C. Analysis of indentation size effect (ISE) behavior in low-load vickers microhardness testing of $(Sm123)_{1-x}(Nd123)_x$ superconductor system. J. Mater. Sci. Mater. El. 2013;24:2218–2227.

75. Dogruer M, Karaboga F, Yildirim G, Terzioglu C, Ozturk O. A comprehensive study on mechanical properties of $Bi_{1.8}Pb_{0.4}Sr_2Mn_xCa_{2.2}Cu_{3.0}O_y$ superconductors. J. Mater. Sci. Mater. El. 2013;24:2659–2666.

76. Dogruer M, Karaboga F, Yildirim G, Terzioglu C. Comparative study on indentation size effect, indentation cracks and superconducting properties of undoped and MgB_2 doped Bi-2223 ceramics. J. Mater. Sci. Mater. El. 2013;24:2327–2338.

77. Turkoz MB, Nezir S, Ozturk O, Asikuzun E, Yildirim G, Terzioglu C, Varilci A. Experimental and theoretical approaches on mechanical evaluation of Y123 system by Lu addition. J. Mater. Sci. Mater. El. 2013;24:2414–2421.

78. Ozturk O, Asikuzun E, Yildirim G. The role of Lu doping on microstructural and superconducting properties of $Bi_2Sr_2CaLu_xCu_2O_y$ superconducting system. J. Mater. Sci. Mater. El. 2013;24:1274–1281.

79. Oliver W, Pharr G. An improved technique for determining hardness and elastic modulus using load and displacement sensing indentation experiments. J. Mater. Res. 1992;6:1564–1583.

80. Zeng K, Chiu CH. An analysis of load-penetration curves from instrumented indentation. Acta Mater. 2001;49:3539–3551.

81. Sangwal K. On the reverse indentation size effect and micro-hardness measurements of solids. Mater. Chem. Phys. 2000;63:145–152.

82. Asikuzun E, Ozturk O, Arda L, Akcan D, Senol SD, Terzioglu C. Preparation, structural and micromechanical properties of (Al/Mg) co-doped ZnO nanoparticles by sol-gel process. J. Mater. Sci. Mater. El. 2015;26:8147–8159.

83. Terzioglu R. The structural and mechanical properties of Gd and Nd substituted double layered $LaCaMnO_7$ ceramics. J. Alloy. Compd. 2019;797:1173–1180.